Automated reconstruction of dendritic and axonal arbors reveals molecular correlates of neuroanatomy

Olga Gliko[1,*], Matt Mallory[1], Rachel Dalley[1], Rohan Gala[1], James Gornet[2], Hongkui Zeng[1], Staci Sorensen[1], and Uygar Sümbül[1,*]

[1]Allen Institute, Seattle WA, USA

[2]California Institute of Technology, Pasadena, CA, USA

[*]Correspondence: olgag@alleninstitute.org, uygars@alleninstitute.org

Abstract

Neuronal anatomy is central to the organization and function of brain cell types. However, anatomical variability within apparently homogeneous populations of cells can obscure such insights. Here, we report large-scale automation of arbor reconstruction on a dataset of 802 inhibitory neurons characterized using the Patch-seq method, which enables measurement of multiple properties from individual neurons, including local morphology and transcriptional signature. We demonstrate that these automated reconstructions can be used in the same manner as manual reconstructions to understand the relationship between many cellular properties used to define cell types. We uncover molecular correlates of laminar innervation on multiple molecularly defined neuronal subclasses and types. In particular, our results reveal molecular correlates of the variability in Layer 1 (L1) innervation even in a transcriptomically defined subpopulation of Martinotti cells in the adult mouse neocortex.

Introduction

The shape of dendrites and axons, their distribution within the neuropil, and patterns of their long-range projections can reveal fundamental principles of nervous system organization and function. In the cortex, much of our understanding depends on the anatomical and functional descriptions of cortical layers. Yet, the origin and role of morphological and molecular diversity of individual neurons within cortical layers beyond broad subclass identities is poorly understood, in part due to low sample numbers. While molecular profiling techniques have recently improved by orders of magnitude, anatomical characterization remains time consuming due to continued reliance on (semi-)manual reconstruction.

Improvements in the throughput of the Patch-seq technique[1–8] have enabled measurement of electrophysiological features, transcriptomic signatures, and local morphology in slice preparations for thousands of neurons in recent studies.[5,6] In these large-scale, sequential experiments, the brightfield microscope's speed, ease of use, and ubiquity make it an attractive choice to image local neuronal arbors. While the experimental steps are streamlined, morphological reconstruction remains a major bottleneck of overall throughput, even with state-of-the-art semi-manual tools.[5] Existing methods that aim to automate reconstruction of neuronal morphology in sparse imaging scenarios typically focus on high-contrast, high-resolution images obtained by confocal, two-photon, and light-sheet microscopy,[9–15] and are not immediately applicable to brightfield images.

Here, we introduce an end-to-end automated neuron reconstruction pipeline to improve scalability of brightfield image-based reconstructions in Patch-seq experiments by a few orders of magnitude. To this end, we curate a set of brightfield images and use the corresponding manually reconstructed neuron traces to assign voxel-wise ground truth labels (axon, dendrite, soma, background). Next, we design a custom deep learning model and train it on this curated ground truth dataset to perform image segmentation using volumetric patches of the raw image as input. We implement fully automated post-processing steps, including basal vs apical dendrite separation for pyramidal cells, for the resulting segmentations to provide annotated traces for each neuron. We compare the accuracy of these automated traces with a held out set of manual reconstructions, based on a suite of features as well as on arbor density representations derived from the traces.

We utilize this pipeline to reconstruct a large set of neurons from Patch-seq experiments, and use the transcriptomic profiles captured from the same cells to systematically search

for gene subsets that can predict subtle aspects of neuronal anatomy. The existence of a hierarchical transcriptomic taxonomy[16] enables studying subsets of neurons at different levels of the transcriptomic hierarchy. At the finest scale of the hierarchy (transcriptomic types or "t-types"[5]), we study five interneuron types and focus on a molecularly homogeneous subpopulation of L1-projecting, Sst+ neurons that correspond to Martinotti cells (e.g., [17]). While previous studies have provided deep insights on the role of Martinotti cells in gating top-down input to pyramidal neurons via their L1-innervating axons,[18,19] the wide variability in the extent of L1 innervation and the mechanism behind it are not well understood. Our results suggest molecular correlates of the innervating axonal mass, which may control the amount of top-down input to canonical cortical circuits. Our approach thus represents a general program to systematically connect gene expression with neuronal anatomy through a combination of multimodal recordings, high-throughput anatomical characterization, and molecular taxonomy in a data-driven manner.

Results

As the first step to automate the reconstruction of in-slice brightfield images of biocytin-filled neurons, we curate a representative set of 51 manually skeletonized neurons. We develop a topology-preserving variant of the fast marching algorithm[11] to generate volumetric labels from arbor traces (Figure 1a). Using these labels as the training set and employing data augmentation strategies, we train a convolutional neural network (U-Net)[13,20–22] to produce initial segmentations of neuronal arbors, and algorithmically post-process those segmentations to correct mistakes introduced by the neural network and obtain the final reconstruction of axons and dendrites (Figure 1b, Supplementary Figures S1– S11, Methods). The overall pipeline produces neuron reconstructions in the commonly-used swc format[23] from raw images at a rate of ∼100 cells/day (Methods). Importantly, this represents two orders of magnitude improvement in speed over semi-manual segmentation[5] with one anatomist. We have so far processed the cells reported in Ref.,[5] which mapped neurons to an existing taxonomy of transcriptomic cell types[16] and introduced a transcription-centric, multimodal analysis of inhibitory neurons. We have also processed a set of ∼800 excitatory neurons which will be analyzed in a forthcoming paper. After quality control steps such as removing cells with incomplete axons (Methods), we focus on a set of 802 interneurons for further study in this paper.

To evaluate the quality of automated reconstructions for cell-type-centric analyses, we first

quantify the accuracy of classical morphometric features calculated from automated reconstructions of a set of test cells. We find that while many features summarizing the overall morphology can be accurately predicted, features related to the topology of arbor shapes, such as maximum branch order, are prone to mistakes (Figure 1c). Therefore, to robustly analyze anatomical innervation patterns against potential topological mistakes introduced by the automated routine, and sidestep the arbitrariness of feature sets and weights, we develop a 2-d arbor density representation (ADR)[10,24–27] of axons and dendrites registered to a common laminar axis defined by cortical pia and white matter boundaries. Here the vertical axis represents the distance from pia and the horizontal axis represents the radial distance from soma (Figure 1d). Figure 1c shows, at the level of transcriptomic types (t-types), that the ADRs calculated from automated reconstructions are very similar to those calculated from manual segmentations.

To further quantify this similarity, we next compare the performance of the ADR against that of morphometric features[28] by training classifiers to predict t-types and subclasses (Sst, Pvalb, Vip, Sncg, Lamp5) for these neurons.[5] We find that the accuracy is very similar between the ADR ($44.3 \pm 6.3\%$ for t-types, $78.1 \pm 5.5\%$ for subclasses, mean $\pm$ s.d.) and morphometric features ($42.9 \pm 3.6\%$ for t-types, $80.6 \pm 2.9\%$ for subclasses),[29] which extends to a high level of cophenetic agreement, as demonstrated by the overall similarity of the confusion matrices (Figure 2a,b, Supplementary Figures S13, S14). Despite mis-classifications of the "leaf nodes" of the hierarchical organization of cell types,[16] the diagonal dominance of both matrices, whose rows and columns are grouped into subclasses and organized based on the reference transcriptomic hierarchy, shows that cells are rarely assigned to distant clusters. This suggests a broad correspondence between RNA expression and the anatomy of local arbors as represented by the proposed registered 2-d ADRs, which agrees with previous findings with morphometric features for these cells.[5] Lastly, we test the robustness of the proposed representations against imperfections due to fully automated tracing by comparing the classification accuracy for ADRs obtained from automated tracing versus manual tracing on the same set of cells. Figure 2c,d suggest that end-to-end automation does not significantly degrade cell type prediction performance. (Supplementary Figure S12 shows a similar result for classification based on morphometric features instead of ADRs.)

Having established that registered 2-d ADRs are as successful as a standardized, rich set of morphometric features in predicting transcriptomic identity and that ADRs can be generated in a fully automated manner without significant performance loss, we study layer-specific axon and dendrite innervation. We treat the search for genes that are predictive of laminar

innervation strength as a sparse regression problem[30,31] (Table 1, Supplementary Tables S1–S3). We find that the sets of laminae innervation-predicting genes within molecularly defined subclasses (Sst, Pvalb, Vip, Lamp5) and terminal, t-types (3 Sst, 2 Pvalb, 2 Lamp5 types) are highly reproducible (Supplementary Table S3) and almost mutually exclusive(Figure 3f). This observation is compatible with laminae representing the dominant axis of cortical organization, and it supports the existence of a connectivity-related, cortical anatomical-molecular logic. It also suggests a related question: can gene expression further predict axonal innervation strength in a continuum within the discrete laminar architecture?

To study this question, we focus on a molecularly homogeneous population that is well-sampled in our dataset, produces a large effect size in the gene regression study (Table 1), and has been a source of confusion due to its anatomical variability: Sst Calb2 Pdlim5 neurons[16] represent a molecularly homogeneous subset of Martinotti cells, which are inhibitory neurons with L1-innervating axons that gate top-down input to pyramidal neurons.[18,19] However, the amount of axon that reaches L1 varies widely across cells.[5] With the help of the diverse set of reconstructions enabled by our automated pipeline, we find that a small subset of genes, including genes implicated in synapse formation, cell-cell recognition and adhesion, and neurite outgrowth and arborization[32–34] (Supplementary Table S3), can nevertheless accurately predict the L1-innervating skeletal mass of neurons belonging to this homogeneous population ($R^2 = 0.40$, $p = 0.02$, non-parametric shuffle test — removing 3 out of 49 cells whose axons don't reach L1 further increases R^2 to 0.51). Since the somata of this population are distributed across L2/3, L4, and L5 (Figure 3a), we next investigate whether the soma depth can explain the variability in L1 innervation. Figure 3b shows a relatively weak correlation between these two variables. Moreover, repeating the sparse regression study after removing the linear contribution of soma depth to L1 innervation still finds a statistically significant predictive power for a small gene subset ($R^2 = 0.29$, $p = 0.02$, non-parametric shuffle test — removing the cells whose axons don't reach L1 produces $R^2 = 0.28$).

Finally, we juxtapose this result with that for the cells of the Lamp5 Lsp1 cell type whose somata are also distributed across multiple cortical layers. In contrast, soma depth almost completely explains the variability in L1 innervation for cells in the Lamp5 Lsp1 population whose axons reach L1 (Figure 3d,e). That is, while Lamp5 Lsp1 cells appear to shift along the laminar axis according to soma location within the cortical depth, soma location does not seem to dictate the axonal L1 innervation of Sst Calb2 Pdlim5 neurons, whose strength can nevertheless be predicted by gene expression. For both of these t-types, the automated reconstruction pipeline increased the sample size by 69%, empowering the statistical analysis

pursued here.

Discussion

While classification of neuronal cell types is increasingly based on single cell and nucleus genomic technologies, characterization of neuron morphology – a classical approach – captures an aspect of neuronal identity that is stable over long time scales, is intimately related to connectivity and function, and can now be connected with genomic attributes through the use of simultaneous profiling techniques such as Patch-seq. Nevertheless, light microscopy based methods of neuronal reconstruction often inadequately reproduce the determinant attributes of morphological signature, especially in high-throughput settings. Here, we have presented an end-to-end automated neuronal arbor reconstruction pipeline for brightfield microscopy, whose simple and ubiquitous setup supports flexible, single or multimodal, characterization protocols. We have also proposed an arbor density representation as a descriptor of cortical neuronal anatomy that is robust against noise in the high-throughput imaging setup as well as mistakes of automated reconstruction.

Through the use of sparsity arguments and statistical testing, we demonstrated that this pipeline can help reveal relationships between gene expression and neuronal anatomy, where a large number of anatomical reconstructions enables accurate inference in the presence of a large gene set. As an application, we studied the correlation between gene expression and laminar innervation on a Patch-seq dataset of cortical neurons[5] and showed that the gene correlates of different innervation patterns have little overlap across molecularly defined subpopulations. While the same program can potentially also address the relationship between morphological and electrophysiological properties of neurons, the accuracy of automated reconstructions should further improve to be used in detailed compartmental models.[35]

Finally, we focused on axonal innervation of L1 by a molecularly defined subpopulation of Somatostatin-expressing Martinotti cells. We found that the innervation strength is relatively weakly correlated with soma depth for this cell type, but not all types. Moreover, a subset of genes can predict the remaining variability in the innervation strength after the effect of soma depth is removed, suggesting a control mechanism beyond simple shifting of the arbor within the cortical depth. Considering that neurons in this population are thought to gate top-down input to cortical pyramidal neurons,[18,19] this result suggests tuning of innervation strength in a

	Sst Calb2 Pdlim5	Sst Hpse Cbln4	Pvalb Reln Itm2a	Pvalb Tpbg	Lamp5 Lsp1
L1 axon	**0.02** / **0.40**	0.46	0.66	0.20	**0.03** / **0.55**
L2/3 axon	**0.03** / **0.31**	1.00	**0.02** / **0.33**	0.21	**0.03** / **0.55**
L4 axon	1.00	**0.03** / 0.23	**0** / **0.43**	0.58	1.00
L5 axon	0.37	0.68	0.67	0.26	1.00
L1 dendrite	0.72	1.00	0.78	**0.02** / **0.40**	1.00
L2/3 dendrite	0.12	1.00	0 / 0.36	0.21	1.00
L4 dendrite	1.00	**0.03** / **0.32**	0.27	1.00	0.58
L5 dendrite	0.07	0.29	**0.02** / **0.30**	**0.03** / **0.39**	1.00
soma depth	0.09	0.53	**0** / **0.43**	**0** / **0.31**	0.05
axon centroid	0.07	1.00	**0** / **0.30**	0.07	**0.04** / **0.43**
dendrite centroid	0.3	0.8	**0** / **0.40**	**0** / **0.36**	0.05

Table 1: Statistical significance and effect size values for predicting anatomical features from gene expression via sparse linear regression for five different cell types. For each entry, the FDR-corrected p-value as calculated by a non-parametric shuffle test is listed. If the value is considered statistically significant at $p < 0.05$, the R^2 value is also displayed (p / R^2). p-values less than 0.05 and R^2 values larger than 0.25 are shown in bold. A p value of 0 indicates that the calculated p value is less than 0.001, the sensitivity of the shuffle test.

continuum within the discrete laminar organization of the mouse cortex, potentially to improve task performance of the underlying neuronal network.

References

[1] Marcela Lipovsek, Cedric Bardy, Cathryn R Cadwell, Kristen Hadley, Dmitry Kobak, and Shreejoy J Tripathy. Patch-seq: Past, present, and future. *Journal of Neuroscience*, 41(5):937–946, 2021.

[2] János Fuzik, Amit Zeisel, Zoltán Máté, Daniela Calvigioni, Yuchio Yanagawa, Gábor Szabó, Sten Linnarsson, and Tibor Harkany. Integration of electrophysiological recordings with single-cell rna-seq data identifies neuronal subtypes. *Nature biotechnology*, 34(2):175, 2016.

[3] Cathryn R Cadwell, Athanasia Palasantza, Xiaolong Jiang, Philipp Berens, Qiaolin Deng, Marlene Yilmaz, Jacob Reimer, Shan Shen, Matthias Bethge, Kimberley F Tolias, et al. Electrophysiological, transcriptomic and morphologic profiling of single neurons using patch-seq. *Nature biotechnology*, 34(2):199–203, 2016.

[4] Csaba Földy, Spyros Darmanis, Jason Aoto, Robert C Malenka, Stephen R Quake, and Thomas C Südhof. Single-cell rnaseq reveals cell adhesion molecule profiles in electrophysiologi-

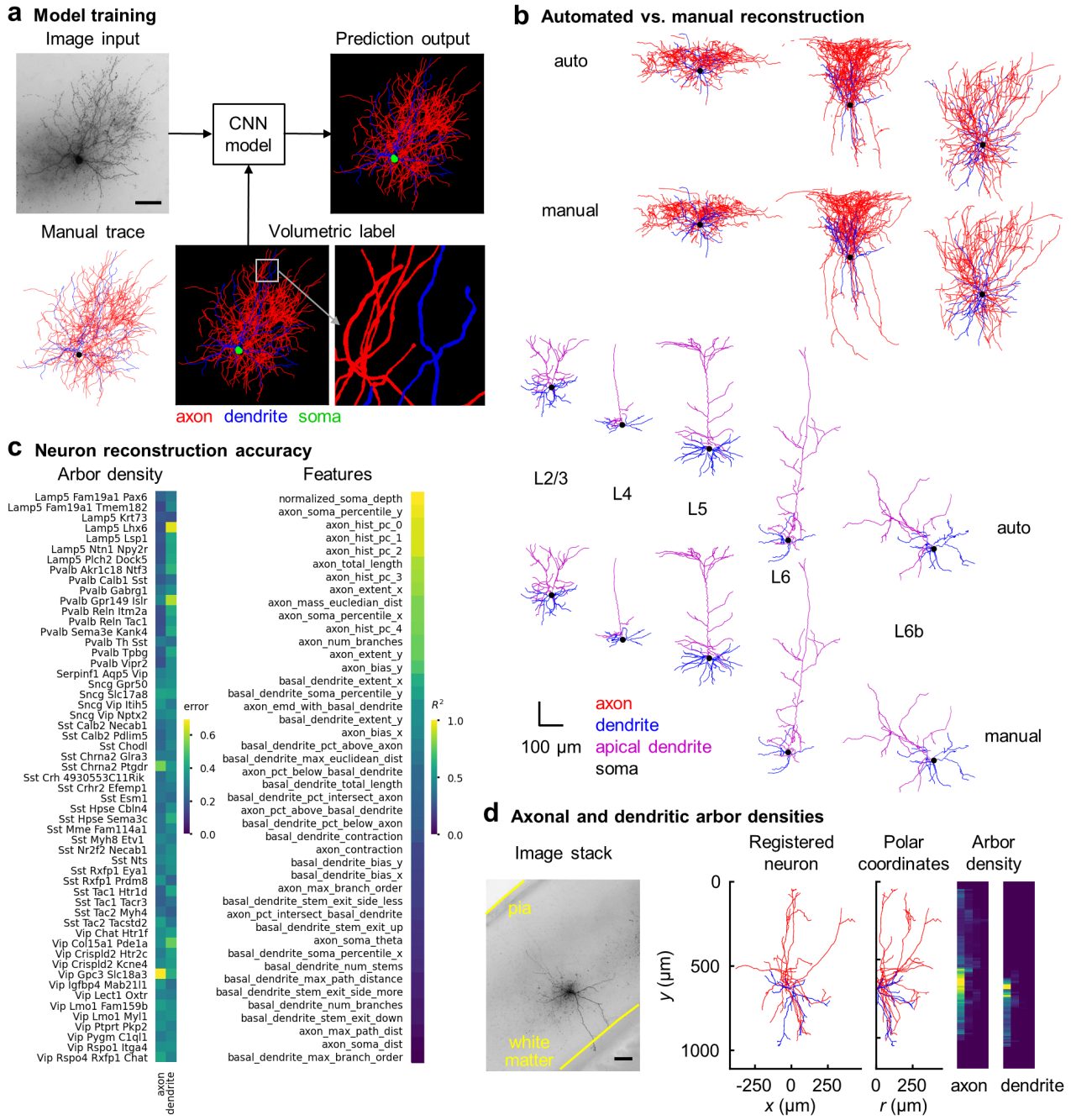

Figure 1: **Neuron reconstruction pipeline for in-slice bright-field images of biocytin-filled neurons.** **a**, Topology preserving fast marching algorithm generates the volumetric label from raw image stack and manual skeletonization. Dendrites (blue), axons (red), soma (green) are separately labeled to train a supervised convolutional neural network (CNN) model. Scale bar, 100 μm. **b**, Segmentations are post-processed to produce digital representations of neuronal arbors. Automated and manual traces of example test neurons are shown (top, inhibitory neurons; bottom, excitatory neurons – apical and basal dendrites are assigned for excitatory cells.) **c**, Root-mean-squared error (left) and R^2 values (right) between automatically vs. manually generated ADRs for each cell type (left) and features (right). ADRs are normalized to have a unit norm. **d**, Generation of 2-d axonal and dendritic ADRs. Scale bar, 100 μm.

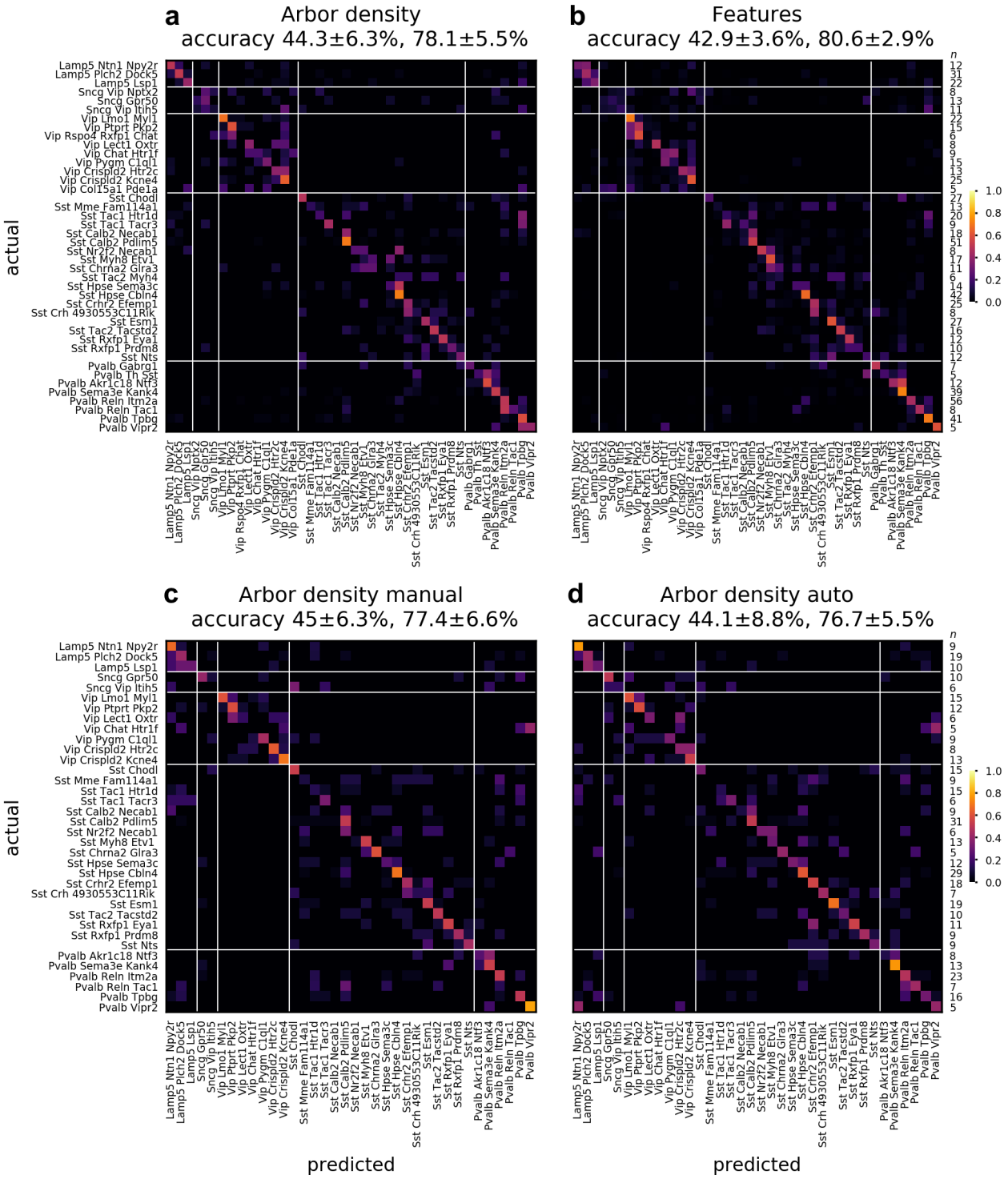

Figure 2: **Comparison of cell type classification accuracy based on the ADR vs a set of classical morphometric features.** Confusion matrix for the classification of t-types based on ADRs (**a**) and morphometric features (**b**), using a combination of 239 automatically and 495 manually reconstructed cells. Confusion matrix for the classification of t-types based on ADRs, using 427 manually (**c**) and automatically (**d**) reconstructed cells. Accuracy values reported in the headers refer to mean ± s.d. of the overall t-type and t-subclass classifiers, respectively, across cross-validation folds. Rightmost columns list the number of cells in each t-type (n).

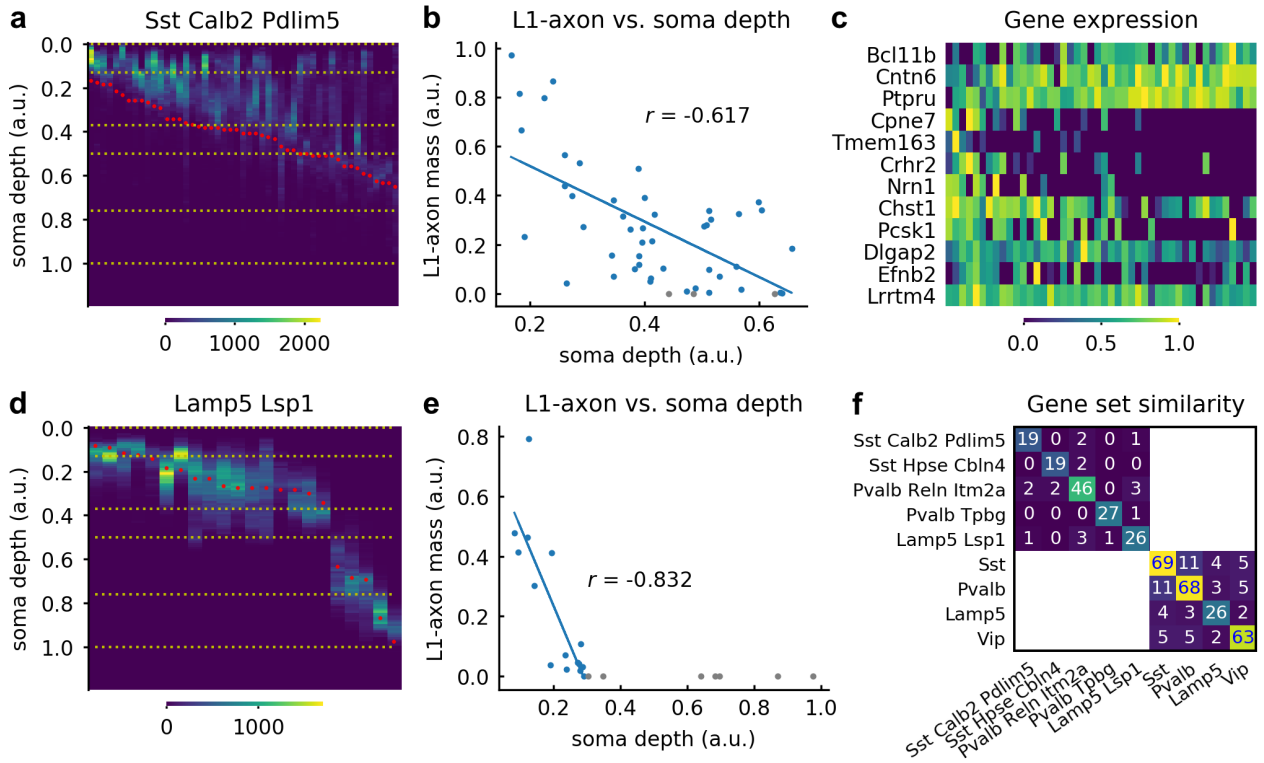

Figure 3: **L1 axonal innervation correlates with expression of subset of genes in Martinotti cells.** 1-d axonal arbor density for the 49 cells in the Sst Calb2 Pdlim5 t-type (**a**) and the 22 cells in the Lamp5 Lsp1 t-type (**d**). Normalized L1-axon skeletal mass vs. soma depth for the Sst Calb2 Pdlim5 cells (**b**) and the Lamp5 Lsp1 cells (**e**). Lines fitted to cells with nonzero L1 innervation. Cells whose axons don't reach L1 are shown in gray. **c**, Gene expression vs. L1-axon skeletal mass for the genes selected by the sparse regression analysis. (L1-axon mass decreases from left to right.) **f**, Similarity matrix for the sets of laminae-predicting genes within transcriptomic types and subclasses. (See Supplementary Table S3.) Each entry denotes the number of genes in the intersection between the corresponding row and column.

cally defined neurons. *Proceedings of the National Academy of Sciences*, 113(35):E5222–E5231, 2016.

[5] Nathan W Gouwens, Staci A Sorensen, Fahimeh Baftizadeh, Agata Budzillo, Brian R Lee, Tim Jarsky, Lauren Alfiler, Katherine Baker, Eliza Barkan, Kyla Berry, et al. Integrated morphoelectric and transcriptomic classification of cortical gabaergic cells. *Cell*, 183(4):935–953, 2020.

[6] Federico Scala, Dmitry Kobak, Matteo Bernabucci, Yves Bernaerts, Cathryn René Cadwell, Jesus Ramon Castro, Leonard Hartmanis, Xiaolong Jiang, Sophie Laturnus, Elanine Miranda, et al. Phenotypic variation of transcriptomic cell types in mouse motor cortex. *Nature*, 598(7879):144–150, 2021.

[7] Brian R Lee, Agata Budzillo, Kristen Hadley, Jeremy A Miller, Tim Jarsky, Katherine Baker, DiJon Hill, Lisa Kim, Rusty Mann, Lindsay Ng, et al. Scaled, high fidelity electrophysiological, morphological, and transcriptomic cell characterization. *Elife*, 10:e65482, 2021.

[8] Lin Que, David Lukacsovich, Wenshu Luo, and Csaba Földy. Transcriptional and morphological profiling of parvalbumin interneuron subpopulations in the mouse hippocampus. *Nature Communications*, 12(1):1–15, 2021.

[9] Engin Türetken, Fethallah Benmansour, and Pascal Fua. Automated reconstruction of tree structures using path classifiers and mixed integer programming. In *2012 IEEE conference on computer vision and pattern recognition*, pages 566–573. IEEE, 2012.

[10] Uygar Sümbül, Sen Song, Kyle McCulloch, Michael Becker, Bin Lin, Joshua R Sanes, Richard H Masland, and H Sebastian Seung. A genetic and computational approach to structurally classify neuronal types. *Nature communications*, 5(1):1–12, 2014.

[11] Rohan Gala, Julio Chapeton, Jayant Jitesh, Chintan Bhavsar, and Armen Stepanyants. Active learning of neuron morphology for accurate automated tracing of neurites. *Frontiers in neuroanatomy*, 8:37, 2014.

[12] Tingwei Quan, Hang Zhou, Jing Li, Shiwei Li, Anan Li, Yuxin Li, Xiaohua Lv, Qingming Luo, Hui Gong, and Shaoqun Zeng. Neurogps-tree: automatic reconstruction of large-scale neuronal populations with dense neurites. *Nature methods*, 13(1):51–54, 2016.

[13] James Gornet, Kannan Umadevi Venkataraju, Arun Narasimhan, Nicholas Turner, Kisuk Lee, H Sebastian Seung, Pavel Osten, and Uygar Sümbül. Reconstructing neuronal anatomy from

whole-brain images. In *2019 IEEE 16th International Symposium on Biomedical Imaging (ISBI 2019)*, pages 218–222. IEEE, 2019.

[14] Johan Winnubst, Erhan Bas, Tiago A Ferreira, Zhuhao Wu, Michael N Economo, Patrick Edson, Ben J Arthur, Christopher Bruns, Konrad Rokicki, David Schauder, et al. Reconstruction of 1,000 projection neurons reveals new cell types and organization of long-range connectivity in the mouse brain. *Cell*, 179(1):268–281, 2019.

[15] Hanchuan Peng, Peng Xie, Lijuan Liu, Xiuli Kuang, Yimin Wang, Lei Qu, Hui Gong, Shengdian Jiang, Anan Li, Zongcai Ruan, et al. Morphological diversity of single neurons in molecularly defined cell types. *Nature*, 598(7879):174–181, 2021.

[16] Bosiljka Tasic, Zizhen Yao, Lucas T Graybuck, Kimberly A Smith, Thuc Nghi Nguyen, Darren Bertagnolli, Jeff Goldy, Emma Garren, Michael N Economo, Sarada Viswanathan, et al. Shared and distinct transcriptomic cell types across neocortical areas. *Nature*, 563(7729):72–78, 2018.

[17] Henry Markram, Eilif Muller, Srikanth Ramaswamy, Michael W Reimann, Marwan Abdellah, Carlos Aguado Sanchez, Anastasia Ailamaki, Lidia Alonso-Nanclares, Nicolas Antille, Selim Arsever, et al. Reconstruction and simulation of neocortical microcircuitry. *Cell*, 163(2):456–492, 2015.

[18] Masanori Murayama, Enrique Pérez-Garci, Thomas Nevian, Tobias Bock, Walter Senn, and Matthew E Larkum. Dendritic encoding of sensory stimuli controlled by deep cortical interneurons. *Nature*, 457(7233):1137, 2009.

[19] Benjamin Schuman, Shlomo Dellal, Alvar Prönneke, Robert Machold, and Bernardo Rudy. Neocortical layer 1: An elegant solution to top-down and bottom-up integration. *Annual Review of Neuroscience*, 44, 2021.

[20] Olaf Ronneberger, Philipp Fischer, and Thomas Brox. U-net: Convolutional networks for biomedical image segmentation. In *International Conference on Medical image computing and computer-assisted intervention*, pages 234–241. Springer, 2015.

[21] Özgün Çiçek, Ahmed Abdulkadir, Soeren S Lienkamp, Thomas Brox, and Olaf Ronneberger. 3d u-net: learning dense volumetric segmentation from sparse annotation. In *International conference on medical image computing and computer-assisted intervention*, pages 424–432. Springer, 2016.

[22] Jan Funke, Fabian Tschopp, William Grisaitis, Arlo Sheridan, Chandan Singh, Stephan Saalfeld, and Srinivas C Turaga. Large scale image segmentation with structured loss based deep learning for connectome reconstruction. *IEEE transactions on pattern analysis and machine intelligence*, 41(7):1669–1680, 2018.

[23] Giorgio A Ascoli. Mobilizing the base of neuroscience data: the case of neuronal morphologies. *Nature Reviews Neuroscience*, 7(4):318–324, 2006.

[24] Armen Stepanyants, Patrick R Hof, and Dmitri B Chklovskii. Geometry and structural plasticity of synaptic connectivity. *Neuron*, 34(2):275–288, 2002.

[25] Hermann Cuntz, Friedrich Forstner, Alexander Borst, and Michael Häusser. One rule to grow them all: a general theory of neuronal branching and its practical application. *PLoS Comput Biol*, 6(8):e1000877, 2010.

[26] Marcel Oberlaender, Christiaan PJ de Kock, Randy M Bruno, Alejandro Ramirez, Hanno S Meyer, Vincent J Dercksen, Moritz Helmstaedter, and Bert Sakmann. Cell type–specific three-dimensional structure of thalamocortical circuits in a column of rat vibrissal cortex. *Cerebral cortex*, 22(10):2375–2391, 2012.

[27] Uygar Sümbül, Aleksandar Zlateski, Ashwin Vishwanathan, Richard H Masland, and H Sebastian Seung. Automated computation of arbor densities: a step toward identifying neuronal cell types. *Frontiers in neuroanatomy*, 8:139, 2014.

[28] NW Gouwens, SA Sorensen, J Berg, C Lee, T Jarsky, J Ting, SM Sunkin, D Feng, CA Anastassiou, E Barkan, K Bickley, N Blesie, T Braun, K Brouner, A Budzillo, S Caldejon, T Casper, D Castelli, P Chong, K Crichton, C Cuhaciyan, TL Daigle, R Dalley, N Dee, T Desta, SL Ding, S Dingman, A Doperalski, N Dotson, T Egdorf, M Fisher, Frates RA de, E Garren, M Garwood, A Gary, N Gaudreault, K Godfrey, M Gorham, H Gu, C Habel, K Hadley, J Harrington, JA Harris, A Henry, D Hill, S Josephsen, S Kebede, L Kim, M Kroll, B Lee, T Lemon, KE Link, X Liu, B Long, R Mann, M McGraw, S Mihalas, A Mukora, GJ Murphy, L Ng, K Ngo, TN Nguyen, PR Nicovich, A Oldre, D Park, S Parry, J Perkins, L Potekhina, D Reid, M Robertson, D Sandman, M Schroedter, C Slaughterbeck, G Soler-Llavina, J Sulc, A Szafer, B Tasic, N Taskin, C Teeter, N Thatra, H Tung, W Wakeman, G Williams, R Young, Z Zhou, C Farrell, H Peng, MJ Hawrylycz, E Lein, L Ng, A Arkhipov, A Bernard, JW Phillips, H Zeng, and C Koch. Classification of electrophysiological and morphological neuron types in the mouse visual cortex. *Nat Neurosci*, 22:1182–1195, Jul 2019.

[29] Sophie Laturnus, Dmitry Kobak, and Philipp Berens. A systematic evaluation of interneuron morphology representations for cell type discrimination. *Neuroinformatics*, 18(4):591–609, 2020.

[30] Ming Yuan and Yi Lin. Model selection and estimation in regression with grouped variables. *Journal of the Royal Statistical Society: Series B (Statistical Methodology)*, 68(1):49–67, 2006.

[31] Dmitry Kobak, Yves Bernaerts, Marissa A Weis, Federico Scala, Andreas S Tolias, and Philipp Berens. Sparse reduced-rank regression for exploratory visualisation of paired multivariate data. *Journal of the Royal Statistical Society: Series C (Applied Statistics)*, 2021.

[32] Akihiro Inoue and Joshua R Sanes. Lamina-specific connectivity in the brain: regulation by n-cadherin, neurotrophins, and glycoconjugates. *Science*, 276(5317):1428–1431, 1997.

[33] Alex L Kolodkin and Marc Tessier-Lavigne. Mechanisms and molecules of neuronal wiring: a primer. *Cold Spring Harbor perspectives in biology*, 3(6):a001727, 2011.

[34] Yu-Chi Sun, Xiaoyin Chen, Stephan Fischer, Shaina Lu, Huiqing Zhan, Jesse Gillis, and Anthony M Zador. Integrating barcoded neuroanatomy with spatial transcriptional profiling enables identification of gene correlates of projections. *Nature Neuroscience*, 2021.

[35] Wulfram Gerstner, Werner M Kistler, Richard Naud, and Liam Paninski. *Neuronal dynamics: From single neurons to networks and models of cognition*. Cambridge University Press, 2014.

[36] Leonard Kuan, Yang Li, Chris Lau, David Feng, Amy Bernard, Susan M Sunkin, Hongkui Zeng, Chinh Dang, Michael Hawrylycz, and Lydia Ng. Neuroinformatics of the allen mouse brain connectivity atlas. *Methods*, 73:4–17, 2015.

[37] Quanxin Wang, Song-Lin Ding, Yang Li, Josh Royall, David Feng, Phil Lesnar, Nile Graddis, Maitham Naeemi, Benjamin Facer, Anh Ho, et al. The allen mouse brain common coordinate framework: a 3d reference atlas. *Cell*, 181(4):936–953, 2020.

[38] James A Sethian. Fast marching methods. *SIAM review*, 41(2):199–235, 1999.

[39] Gilles Bertrand and Grégoire Malandain. A new characterization of three-dimensional simple points. *Pattern Recognition Letters*, 15(2):169–175, 1994.

[40] Diederik P Kingma and Jimmy Ba. Adam: A method for stochastic optimization. *arXiv preprint arXiv:1412.6980*, 2014.

[41] F. Pedregosa, G. Varoquaux, A. Gramfort, V. Michel, B. Thirion, O. Grisel, M. Blondel, P. Prettenhofer, R. Weiss, V. Dubourg, J. Vanderplas, A. Passos, D. Cournapeau, M. Brucher, M. Perrot, and E. Duchesnay. Scikit-learn: Machine learning in Python. *Journal of Machine Learning Research*, 12:2825–2830, 2011.

[42] Stephen J Smith, Uygar Sümbül, Lucas T Graybuck, Forrest Collman, Sharmishtaa Seshamani, Rohan Gala, Olga Gliko, Leila Elabbady, Jeremy A Miller, Trygve E Bakken, et al. Single-cell transcriptomic evidence for dense intracortical neuropeptide networks. *Elife*, 8:e47889, 2019.

[43] Rohan Gala, Agata Budzillo, Fahimeh Baftizadeh, Jeremy Miller, Nathan Gouwens, Anton Arkhipov, Gabe Murphy, Bosiljka Tasic, Hongkui Zeng, Michael Hawrylycz, et al. Consistent cross-modal identification of cortical neurons with coupled autoencoders. *Nature Computational Science*, 1(2):120–127, 2021.

[44] Trygve E Bakken, Rebecca D Hodge, Jeremy A Miller, Zizhen Yao, Thuc Nghi Nguyen, Brian Aevermann, Eliza Barkan, Darren Bertagnolli, Tamara Casper, Nick Dee, et al. Single-nucleus and single-cell transcriptomes compared in matched cortical cell types. *PloS one*, 13(12):e0209648, 2018.

[45] Robert Tibshirani. Regression shrinkage and selection via the lasso. *Journal of the Royal Statistical Society: Series B (Methodological)*, 58(1):267–288, 1996.

[46] Yoav Benjamini and Daniel Yekutieli. The control of the false discovery rate in multiple testing under dependency. *Annals of statistics*, pages 1165–1188, 2001.

[47] Skipper Seabold and Josef Perktold. statsmodels: Econometric and statistical modeling with python. In *9th Python in Science Conference*, 2010.

Methods

Dataset

The dataset profiling local morphology and transcriptome of GABAergic mouse visual cortical neurons was generated as part of the Patch-seq recordings described in Ref.[5] This dataset includes 2,341 cells with transcriptomic profiling and high resolution image stacks, where the brain sections were imaged on an upright AxioImager Z2 microscope (Zeiss) equipped with an Axiocam506 monochrome camera. Tiled image stacks of individual cells were acquired with a

63× objective lens (Zeiss Plan-Apochromat 63×/1.4 NA or Zeiss LD LCI Plan-Apochromat 63×/1.2 NA) at an interval of 0.28 μm or 0.44 μm along the Z axis. Individual cells were manually placed in the appropriate cortical region and layer within the Allen Mouse Common Coordinate Framework (CCF)[36,37] by matching the 20X image of the slice with a "virtual" slice at an appropriate location and orientation within the CCF. 1,259 cells were removed from the dataset either because they were mapped to nearby regions (instead of visual cortex) or because their images had incomplete axons. 537 of the remaining 1,082 bright-field image stacks of biocytin-filled neurons were reconstructed both manually and automatically, and this set is used for training and testing of the t-type classification algorithms and for error/R^2-value quantification. The remaining 545 cells were reconstructed only automatically. To ensure the quality of scientific results presented in Table 1 and Figure 3, we excluded 117 images with multiple neurons in the field of view and 151 images that failed at different stages of the pipeline (missing pia/white matter annotations, annotation-related failed upright transformation, reconstruction failing visual inspection) from those analyses. Finally, 94 cells in the manually and automatically reconstructed population and 45 cells in the automatically-only reconstructed population were not used for analyses involving t-types because these cells were deemed to not have "highly consistent" t-type mappings in Ref.[5]

Volumetric training data generation from skeletonized arbors

Segmentation of neuronal arbors from 3-d image stack requires voxel-wise labels while manual reconstructions specified by traces only provide a set of vertices and edges corresponding to the layout of the underlying arbor. We developed a topology preserving fast marching algorithm to generate volumetric ground truth using raw image stacks and manual traces. We adapted a fast-marching based segmentation algorithm[11,38] initialized with trace vertices to segment image voxels. This segmentation should be consistent with the layout of traced arbors, without introducing topological errors (e.g., splits, merges, holes). This is ensured by incorporating simple point methods in digital topology[39] into the segmentation algorithm. We noticed that the soma can be incompletely filled by the fastmarching algorithm. Therefore, we treated the soma region separately and used a sequence of erosion and dilation operations followed by manual thresholding to achieve complete labeling. Each voxel was labeled as axon, dendrite, soma, background for interneurons.

Neural network architecture and training

We used a 3-d U-Net convolutional neural network[21] to perform multi-class segmentation (i.e. each voxel is assigned a probability of belonging to classes specified in the label set). We trained two separate models using raw images and volumetric ground truth; one with 51 inhibitory neurons, and with 75 excitatory neurons from mouse cortex. The U-Net architecture consists of a contracting path to capture context and a symmetric expanding path that enables precise localization and has been shown to achieve state-of-the-art performance in many segmentation tasks.[20,21] Building on previous work,[13] we developed an efficient Pytorch implementation that runs on graphical processing units (GPUs). To address GPU memory constraints, during each training epoch the training set was divided randomly into subsets of 3 stacks. Training proceeded sequentially using all subsets in an epoch, and data loading time did not exceed 10% of the total training time. We trained the model on batches of 3-d patches ($128 \times 128 \times 32$ px^3, XYZ), which were randomly sampled from the subset of 3 stacks loaded into memory. All the models were trained using the Adam optimizer[40] with a learning rate of 0.1. Training with a GeForce GTX 1080 GPU for ~ 50 epochs took ~ 3 weeks. Since the neuron occupies a small fraction of the image volume, we chose patches that contained at least one voxel belonging to the neuron. To add salient, negative examples to the training set, we also included a number of patches with bright backgrounds produced by staining artifacts and pial surface. To enable the model to generalize from relatively small number of training examples and improve the segmentation accuracy, we augmented training data by 90° rotations and vertical/horizontal flips in the image (XY) plane.

End-to-end neuron reconstruction pipeline

An end-to-end automated pipeline combined segmentation of raw image stacks into soma, axon, and dendrite structures with post-processing routines to produce a swc file. Segmentation with trained models using a single high-end GPU takes ∼5.8 min per Gvoxel, or ∼186 min for average 32 Gvoxel image stack. Our pipeline had access to 16 GPU (NVIDIA Titan X) cards. Even though model trained using inhibitory neurons generalized well on all type of neurons, we found model trained using excitatory neurons to have improved axon/dendrite assignment on excitatory neurons. Segmentation was post-processed by thresholding background, followed by connected component analysis to remove short segments, skeletonization, connecting broken segments and converting to digital reconstruction in swc format.

Reconstructions were passed through a series of additional post-processing including extraneous cell/artefact removal, down sampling, node sorting and pruning. We trained a random forest classifier to identify apical dendrite segments in excitatory auto-trace reconstructions. The classifier was trained on geometric features that distinguish apical dendrite segments from basal dendrite (e.g. upright distance from soma). The classifier achieved a mean accuracy of 85% percent across 10-fold cross validation. When available, manual reconstructions were used to mask extraneous cells or artefacts that were not removed during post-processing.

Reconstructions were transformed to an upright position that is perpendicular with respect to pia and white matter surfaces. Morphological features as described in[28] were calculated using the neuron_morphology python package. To minimize technical artefacts introduced by sample compression after processing, z-dimension features were not analyzed.

Arbor density generation of axons and dendrites

We represented axonal and dendritic arbors as 2-d density maps registered to a common local coordinate axis using the pia/white matter boundaries. First, we applied upright transform to the reconstructed neuron followed by the correction of z-shrinkage and the variable tilt angle of the acute slice.[28] Next, adapting our previous work[10,27] we conformally mapped pia and white matter boundaries to flat surfaces, calculated a nonlinear transformation on the whole tissue by a least-square fit to pia/white matter mappings, and applied this transformation to the neural arbor. Finally, we used the registered neuronal arbor to generate a 2-d density representation. The polar axes representing the cortical depth and the lateral distance from the soma (Figure 1d) make this representation invariant to rotations around the laminar axis. We calculated these maps separately for axons and dendrites. We downsampled these maps to 120px $\times$ 4px images with a pixel size of $8\mu m \times 125\mu m$ to be robust to minor changes in arbor shapes. We normalized the intensity by the lateral area corresponding to each pixel so that each pixel value represents local arbor density.

Assessing neuron reconstruction accuracy

To assess the quality of automated neuron reconstructions we calculated the accuracy of morphometric features and ADRs for a set of test cells. We reported the correlation coefficient R^2 for each morphometric feature. We calculated a root-mean-squared error between normalized

axon/dendrite ADRs derived from automated and manual reconstructions and reported it for each transcriptomic type.

Supervised classification

Supervised classification using morphological features was performed by training a random forest classifier implemented in the scikit-learn Python package.[41] Supervised classification using ADRs was done by training a feed-forward neural network classifier. The network architecture consists of a convolutional layer with 7x3x1 filter, a 4x1x1 max pool, a convolutional layer with 7x3x1 filter, a 3x1x1 max pool, a concatenation layer with soma depth, and a fully connected layer with number of units corresponding to the number of classes. Each convolutional layer uses the rectified linear function as the non-linear transformation. We apply novel data augmentation strategies including cell type dependent random shift of the ADR and the soma depth in the laminar direction, and a modulation of the intensity values of the ADR. The networks were trained using the cross-entropy loss function and the Adam optimizer with a learning rate of 0.001. Training using Pytorch implementation using GeForce GTX 1080 GPU for 50,000 epochs took $\sim$ 24 h. A set of 239 automatically and 495 manually reconstructed cells was used for training classifiers shown in Figure 2a and b, and a set of the same 427 automatically and manually reconstructed cells were used for Figure 2c and d and Supplementary Figure S12. Both sets included only cells from t-types with at least 5 cells. Confusion matrices, mean and standard deviation of accuracy across cross-validation folds were reported.

Cophenetic agreement: To take the hierarchical organization of transcriptomically defined mouse cortical cell types[16] into account when evaluating the accuracies of the different classification tasks, we defined resolution index per cell as the scaled height of the closest common ancestor of assigned and predicted labels in the t-type hierarchical tree[42] (Supplementary Figures S13 and S14). Accordingly, the resolution index for a correctly classified t-type ("leaf node" label) is 1. In the worst case, the closest ancestor for an assigned and predicted label can be the root node of the taxonomy, which corresponds to a resolution index of 0. We report the mean and s.e.m. values for this measure of cophenetic agreement between true and predicted assignments for each cell type in Supplementary Figures S13 and S14.

Sparse feature selection analysis

Following Ref.,[43] a set of 1,252 genes were used for this analysis. This set was obtained by excluding genes if they satisfy any of the following criteria: (1) they are highly expressed in non-neuronal cells, (2) they have previously reported sex or mitochondrial associations, and (3) they are much more highly expressed in Patch-seq data vs. Fluorescence Activated Cell Sorting (FACS) data (or vice versa) and therefore may be associated with the experimental platform[5]. Further, we removed gene models and some other families of unannotated genes that may be difficult to interpret. We also used the β score, a published measure to evaluate the degree to which gene expression is exclusive to t-types,[44] to exclude genes expressed broadly across t-types. Gene expression values were CPM normalized, and then $\log_e(\bullet + 1)$ transformed for all the downstream analyses.

A set of 681 neurons was used for the feature selection analysis where automated reconstructions comprise $\sim 34\%$ of this set ($\sim 50\%$ of the subset of 7 t-types studied in Figure 3). Every neuron in the dataset was characterized by the expression levels of the set of 1252 genes, and their axonal and dendritic 1-d arbor density representations were organized into two 120×1 vectors. For each neuron, axon/dendrite layer-specific skeletal masses normalized by total skeletal mass were calculated to quantify layer-specific innervation for axonal and dendritic arbors, and axon/dendrite centroids were calculated to characterize laminar position of arbor. To select a small subset of genes that are responsible for the variability in individual anatomical features within each transcriptomic type or subclass, we solved the Lasso regression problem[45] (LassoCV command in the scikit-learn library[41]) for each anatomical feature using the cells in that transcriptomic set. We analyzed only the sets corresponding to the types and subclasses with at least 20 cells. Briefly, let K_t denote the number of cells of type or subclass t for which we have both anatomical features y_t (a $K_t \times 1$ vector) and gene expression values X_t (a $K_t \times N$ matrix). We solve

$$\text{minimize } \frac{1}{2K_t}\|y_t - X_t w_t\|_2^2 + \alpha\|w_t\|_1$$

by performing nested 5-fold cross-validation. For each cross-validation fold, we passed the training set into LassoCV which performed another splitting of the data to determine the hyperparameter α and the set of selected genes. We selected the 10 genes with maximum absolute weight values and calculated the coefficient of determination, R^2, for the test set. Finally, we selected the 10 most frequent genes across the 5 folds and calculated the mean test R^2 value. To evaluate statistical significance, we shuffled the rows of the gene expression matrix X_t 1000 times and used the same procedure to calculate mean test R^2 value for each shuffled

run. We calculated the one-sided p-value as the fraction of shuffled runs with R^2 values greater than or equal to the true R^2. Finally, we performed multiple testing correction of p-values using Benjamini-Yekutieli method[46] to control the fast discovery rate (multipletests command in the statsmodels library[47]). We report resulting p-values and test R^2 values for selected t-types in Table 1 and for the expanded set of t-types and subclasses in Supplementary Tables S1 and S2.

Data availability

Transcriptomic and morphological data supporting the findings of this study is available online at `https://portal.brain-map.org/explore/classes/multimodal-characterization` ("Neurons in Mouse Primary Visual Cortex").

Code availability

Code pertaining to this study as well as the trained neural network model for automated segmentation are available at `https://github.com/ogliko/patchseq-autorecon` and `https://github.com/rhngla/topo-preserve-fastmarching`.

Acknowledgements

We wish to thank the Allen Institute for Brain Science founder, Paul G Allen, for his vision, encouragement and support. We thank Michael Hawrylycz and Claire Gamlin for helpful feedback on the manuscript. This work was supported by the National Institute Of Mental Health of the National Institutes of Health under award numbers 1U01MH114824-01 and 1RF1MH128778-01. The content is solely the responsibility of the authors and does not necessarily represent the official views of the National Institutes of Health.

Competing Interests

The authors declare no competing interests.

Supplementary Materials

	Sst Calb2 Pdlim5	Sst Hpse Cbln4	Sst Chodl	Pvalb Reln Itm2a	Pvalb Tpbg	Lamp5 Lsp1
L1 axon	**1.59e-2** / **0.40**	4.63e-1	1.00e-0	6.62e-1	1.95e-1	**2.83e-2** / **0.55**
L2/3 axon	**2.83e-2** / **0.31**	1.00e-0	1.00e-0	**1.59e-2** / **0.33**	2.09e-1	**2.83e-2** / **0.55**
L4 axon	1.00e-0	**2.83e-2** / 0.23	1.00e-0	**0** / **0.43**	5.84e-1	1.00e-0
L5 axon	3.73e-1	6.81e-1	1.00e-0	6.71e-1	2.64e-1	1.00e-0
L6 axon	2.16e-1	3.40e-1	1.00e-0	1.00e-0	5.17e-1	7.43e-2
L1 dendrite	7.21e-1	1.00e-0	1.00e-0	7.77e-1	**1.59e-2** / **0.40**	1.00e-0
L2/3 dendrite	1.18e-1	1.00e-0	4.50e-1	**0** / **0.36**	2.09e-1	1.00e-0
L4 dendrite	1.00e-0	**2.83e-2** / **0.32**	4.79e-1	2.71e-1	1.00e-0	5.82e-1
L5 dendrite	6.50e-2	2.87e-1	1.00e-0	**1.59e-2** / **0.30**	**2.83e-2** / **0.39**	1.00e-0
L6 dendrite	1.84e-1	1.00e-0	7.85e-1	2.09e-1	1.00e-0	1.00e-0
soma depth	8.53e-2	5.28e-1	3.92e-1	**0** / **0.43**	**0** / **0.31**	5.37e-2
axon centroid	6.50e-2	1.00e-0	1.90e-1	**0** / **0.30**	7.43e-2	**4.17e-2** / **0.43**
dendrite centroid	3.15e-1	8.43e-1	1.90e-1	**0** / **0.40**	**0** / **0.36**	5.37e-2

	Lamp5 Plch2 Dock5	Sst	Pvalb	Lamp5	Vip
L1 axon	7.43e-2	**0** / 0.23	**0** / **0.36**	**0** / **0.40**	**0** / **0.40**
L2/3 axon	3.09e-1	**0** / **0.43**	**0** / **0.59**	1.00e-0	**0** / **0.27**
L4 axon	1.00e-0	**0** / **0.40**	**0** / **0.38**	1.63e-1	**1.59e-2** / 0.12
L5 axon	1.00e-0	**0** / **0.33**	**0** / 0.12	1.00e-0	**0** / 0.20
L6 axon	1.95e-1	**0** / **0.37**	**0** / **0.51**	1.00e-0	2.94e-1
L1 dendrite	3.92e-1	1.00e-0	**0** / **0.27**	9.60e-2	6.28e-1
L2/3 dendrite	1.00e-0	**0** / **0.37**	**0** / **0.56**	1.00e-0	**0** / **0.49**
L4 dendrite	1.00e-0	**0** / **0.39**	**0** / **0.28**	1.00e-0	**0** / 0.21
L5 dendrite	7.69e-1	**0** / 0.17	**0** / 0.18	1.00e-0	**0** / **0.30**
L6 dendrite	1.00e-0	**0** / **0.42**	**0** / **0.53**	4.79e-1	1.00e-0
soma depth	1.00e-0	**0** / **0.36**	**0** / **0.71**	**0** / 0.21	**0** / 0.23
axon centroid	7.93e-1	**0** / **0.57**	**0** / **0.71**	**0** / **0.26**	**0** / 0.23
dendrite centroid	1.00e-0	**0** / **0.47**	**0** / **0.67**	**0** / 0.24	**0** / **0.25**

Table S1: Statistical significance and effect size values for predicting anatomical features from gene expression via sparse linear regression for seven different cell types and four subclasses. For each entry, the FDR-corrected p-value as calculated by a non-parametric shuffle test is listed. (See Sparse feature selection analysis under Methods.) If the value is considered statistically significant at $p < 0.05$, the R^2 value is also displayed (p / R^2). p-values less than 0.05 and R^2 values larger than 0.25 are shown in bold.

	Sst Calb2 Pdlim5	Sst Hpse Cbln4	Sst Chodl	Pvalb Reln Itm2a	Pvalb Tpbg	Lamp5 Lsp1
L1 axon	**1.00e-3** / **0.40**	5.20e-2	2.43e-1	8.10e-2	**1.80e-2** / 0.15	**2.00e-3** / **0.55**
L2/3 axon	**2.03e-3** / **0.31**	4.38e-1	3.61e-1	**1.00e-3** / **0.33**	**2.00e-2** / 0.10	**2.00e-3** / **0.55**
L4 axon	2.03e-1	**2.00e-3** / 0.23	1.87e-1	**0** / **0.43**	7.00e-2	4.39e-1
L5 axon	**4.00e-2** / 0.07	8.50e-2	2.09e-1	8.30e-2	**2.6e-2** / 0.05	3.44e-1
L6 axon	**2.10e-2** / 0.05	**3.60e-2** / 0.06	1.69e-1	6.62e-1	6.00e-2	**6.00e-3** / **0.33**
L1 dendrite	9.10e-2	4.34e-1	2.53e-1	1.00e-1	**1.00e-3** / **0.40**	4.03e-1
L2/3 dendrite	**1.00e-2** / 0.21	1.54e-1	**5.00e-2** / 0	**0** / **0.36**	**2.00e-2** / 0.15	3.09e-1
L4 dendrite	2.05e-1	**2.00e-3** / **0.32**	5.50e-2	**2.70e-2** / 0.08	3.52e-1	6.90e-2
L5 dendrite	**5.00e-3** / 0.22	**2.90e-2** / 0.12	4.27e-1	**1.00e-3** / **0.30**	**2.00e-3** / **0.39**	1.43e-1
L6 dendrite	**1.60e-2** / 0.02	1.40e-1	1.02e-1	**2.00e-2** / 0.07	2.80e-2	2.53e-1
soma depth	**7.00e-3** / 0.18	6.20e-2	**4.30e-2** / 0.15	**0** / **0.43**	**0** / **0.31**	**4.00e-3** / **0.42**
axon centroid	**5.00e-3** / **0.26**	1.97e-1	**1.70e-2** / **0.34**	**0** / **0.30**	**6.00e-3** / **0.27**	**3.00e-3** / **0.43**
dendrite centroid	**3.30e-2** / 0.12	1.11e-1	**1.70e-2** / **0.30**	**0** / **0.40**	**0** / **0.36**	**4.00e-3** / **0.41**
	Lamp5 Plch2 Dock5	Sst	Pvalb	Lamp5	Vip	
L1 axon	**6.00e-3** / **0.42**	**0** / 0.23	**0** / **0.36**	**0** / **0.40**	**0** / **0.40**	
L2/3 axon	**3.20e-2** / 0.18	**0** / **0.43**	**0** / **0.59**	7.63e-1	**0** / **0.27**	
L4 axon	1.63e-1	**0** / **0.40**	**0** / **0.38**	**1.40e-2** / 0.09	**1.00e-3** / 0.12	
L5 axon	1.49e-1	**0** / **0.33**	**0** / 0.12	3.25e-1	**0** / 0.20	
L6 axon	**1.80e-2** / 0.08	**0** / **0.37**	**0** / **0.51**	2.69e-1	**3.00e-2** / -0.07	
L1 dendrite	**4.30e-2** / 0.16	6.00e-1	**0** / **0.27**	**8.00e-3** / 0.11	7.60e-2	
L2/3 dendrite	2.50e-1	**0** / **0.37**	**0** / **0.56**	6.07e-1	**0** / **0.49**	
L4 dendrite	2.39e-1	**0** / **0.39**	**0** / **0.28**	2.06e-1	**0** / 0.21	
L5 dendrite	9.80e-2	**0** / 0.17	**0** / 0.18	2.85e-1	**0** / **0.30**	
L6 dendrite	1.46e-1	**0** / **0.42**	**0** / **0.53**	5.50e-2	2.90e-1	
soma depth	2.49e-1	**0** / **0.36**	**0** / **0.71**	**0** / 0.21	**0** / 0.23	
axon centroid	1.04e-1	**0** / **0.57**	**0** / **0.71**	**0** / **0.26**	**0** / 0.23	
dendrite centroid	3.65e-1	**0** / **0.47**	**0** / **0.67**	**0** / 0.24	**0** / **0.25**	

Table S2: Statistical significance and effect size values for predicting anatomical features from gene expression via sparse linear regression for seven different cell types and four subclasses. For each entry, original p-value as calculated by a non-parametric shuffle test is listed. If the value is considered statistically significant at $p < 0.05$, the R^2 value is also displayed (p / R^2). p-values less than 0.05 and R^2 values larger than 0.25 are shown in bold.

Population	Feature	Genes
Sst Calb2 Pdlim5	L1 axon	Bcl11b (5), Cntn6 (4), Ptpru (4), Cpne7 (4), Tmem163 (4), Crhr2 (3), Nrn1 (3), Chst1 (2), Pcsk1 (2), Dlgap2 (1)
Sst Calb2 Pdlim5	L2/3 axon	Cacng5 (5), Kcnq5 (5), Tmem163 (4), Arc (4), Vav2 (3), Cst6 (3), Ildr2 (3), Arhgef3 (2), Myzap (2), Kcnh3 (2)
Sst Hpse Cbln4	L4 axon	LOC105245487 (4), Syndig1l (4), Dner (4), Egfem1 (4), Pde9a (2), Calb2 (2), Gfpt2 (2), Gjd2 (2), Vat1l (2), Arhgap24 (2)
Sst Hpse Cbln4	L4 dendrite	Hpse (4), Kcnab1 (4), Epha3 (3), Timp2 (3), Htr1a (3), Vat1l (3), Rims3 (2), Cux2 (2), Sec14l2 (2), Map3k5 (2)
Pvalb Reln Itm2a	L2/3 axon	Sertad1 (4), Vav2 (3), Cort (3), Hrh1 (3), Kcnd3 (3), Ncam2 (3), Rgs6 (2), Lrrtm4 (2), Nell2 (2), LOC105244192 (2)
Pvalb Reln Itm2a	L4 axon	Cdh9 (5), Cort (5), Kcnk3 (4), Lrrc3b (4), Stac2 (4), Tcap (3), Parm1 (2), Pkib (2), Cplx2 (1), Ephb1 (1)
Pvalb Reln Itm2a	L2/3 dendrite	Cntn5 (5), Sertad1 (4), Kcnd3 (4), Ncam2 (3), Brinp3 (3), Col25a1 (3), Vax1 (2), Cux2 (2), Fstl4 (2), Galntl6 (2)
Pvalb Reln Itm2a	L5 dendrite	Galntl6 (5), Ano3 (4), Adra1a (3), Slc26a4 (3), Kcnip4 (3), Rcan3 (3), Nrtn (3), Gabrg1 (2), Lrrtm4 (2), Sema3a (2)
Pvalb Reln Itm2a	soma depth	Npas3 (5), Grm7 (4), Thsd7a (3), Kcnd3 (3), Galntl6 (3), Tox (2), Hpse (2), Cntn5 (2), Ppapdc1a (2), Opcml (2)
Pvalb Reln Itm2a	axon centroid	Tox (5), Thsd7a (5), Opcml (4), Cntn5 (4), Sptbn5 (3), Sertad1 (3), Cdh22 (3), Npas3 (3), Atp2b4 (2), Rgs6 (2)
Pvalb Reln Itm2a	dendrite centroid	Brinp3 (5), Thsd7a (4), Galntl6 (4), Opcml (4), Cntn5 (3), Cntn6 (3), Kcnd3 (3), Lrrc6 (2), Kcnip4 (2), Hpse (2)
Pvalb Tpbg	L1 dendrite	Nos1 (4), Itpka (4), Mrap2 (4), LOC102636041 (3), Zar1l (2), Cnih3 (2), Hrk (2), Igf1 (2), Iqgap2 (2), Sphkap (2)
Pvalb Tpbg	L5 dendrite	9630002D21Rik (5), Slc10a4 (4), Sfrp2 (4), Tnnt1 (3), Spint2 (3), Calb1 (2), Cd24a (2), Tmem150c (2), LOC105243542 (2), Hs3st4 (2)
Pvalb Tpbg	soma depth	Nxph1 (5), Osbpl3 (4), 9630002D21Rik (4), Sfrp2 (3), Nos1 (3), LOC105243542 (2), Myh7 (2), Klhdc8a (2), BC048546 (2), 6330403K07Rik (2)
Pvalb Tpbg	dendrite centroid	Osbpl3 (5), 9630002D21Rik (4), Itpka (4), Nxph1 (4), Hs3st4 (3), Klhdc8a (3), LOC105243542 (3), Myh7 (3), Nos1 (2), Medag (2)
Lamp5 Lsp1	L1 axon	Dusp14 (5), March11 (4), Nptxr (4), Glce (3), Rasal1 (3), Pou3f3 (3), Ndst4 (2), Kcnip4 (2), Mgat4c (2), Fhod3 (2)
Lamp5 Lsp1	L2/3 axon	Sertad1 (5), Hunk (4), Sulf1 (3), Pbx3 (3), 3300002P13Rik (2), Sdk2 (2), Bcl11b (2), Elavl2 (2), Klf10 (1), Itga8 (1)
Lamp5 Lsp1	axon centroid	Adra1b (4), Dusp14 (4), Rnf152 (4), Sulf1 (3), Spats2l (3), Pde1a (3), LOC105243542 (3), Pou3f3 (2), Pbx3 (2), Nell2 (2)
Sst	L1 axon	Mgat4c (5), Npy2r (5), Kcnip4 (4), P2ry1 (4), Atp2b4 (4), Myh7 (4), Mrap2 (4), Thsd7a (3), Pcsk5 (2), Olfm3 (2)
Sst	L2/3 axon	Thsd7a (5), Rgs9 (5), Grik1 (5), Akr1c18 (4), Mgat4c (4), Col11a1 (4), Rxfp3 (3), Cacng5 (3), Ajap1 (2), Fstl4 (2)
Sst	L4 axon	Syndig1l (5), Clstn2 (5), Npnt (5), Hpse (5), Lrrtm4 (4), Rerg (4), Cort (3), Tmem132d (3), Kcnab1 (2), Crhr2 (2)
Sst	L5 axon	Grm1 (5), Sema3e (5), Arc (4), Olfm3 (4), Col11a1 (4), Mgat4c (3), Nrgn (3), Zfp536 (3), Spon1 (2), Lypd6 (2)
Sst	L6 axon	Penk (5), Col6a1 (5), Sp8 (4), Ptpru (4), Kirrel3 (4), Grik1 (4), Dpp10 (4), Sorcs3 (3), Itga8 (2), Crygs (2)
Sst	L2/3 dendrite	Mgat4c (5), Npy2r (5), Cbln4 (5), Grm1 (5), Dab1 (4), Ajap1 (4), Rgs9 (3), Mrap2 (3), LOC105244376 (2), Grik1 (2)
Sst	L4 dendrite	Hpse (5), Lypd6b (5), Col11a1 (5), Gabrg3 (5), Lypd6 (4), Epha3 (3), Syndig1l (3), Hdac9 (2), Grik1 (2), Rerg (2)
Sst	L5 dendrite	Zfp536 (5), Grm1 (5), Sel1l3 (4), C1qtnf7 (3), Npy2r (3), Gfra2 (3), Kcnk3 (2), Cckbr (2), Cntnap5c (2), Fat3 (2)
Sst	L6 dendrite	Kirrel3 (5), Col6a1 (5), Syndig1 (4), Sorcs3 (4), Olfm3 (4), Grik1 (4), Grm8 (3), Crhr2 (2), Crym (2), Fam19a5 (2)
Sst	soma depth	Unc5d (4), LOC105242740 (4), Cidea (4), Fam19a5 (4), Olfm3 (4), Syndig1 (3), Kirrel3 (3), Nmbr (3), Cpne7 (2), Crym (2)
Sst	axon centroid	Thsd7a (5), Olfm3 (5), Mgat4c (5), Kirrel3 (5), Grik1 (5), Car10 (5), Unc5d (4), Sorcs3 (4), Lypd6 (4), Ano3 (2)
Sst	dendrite centroid	Grik1 (5), Npy2r (5), Mgat4c (5), Car10 (4), Olfm3 (4), Lypd6 (3), Col11a1 (3), Kirrel3 (3), Lypd6b (3), Thsd7a (2)
Pvalb	L1 axon	Rgs14 (5), Col25a1 (5), Myh7 (4), LOC102636041 (3), Etv1 (3), Igf1 (3), Itpka (3), 2010300C02Rik (3), LOC102636700 (3), Necab1 (2)
Pvalb	L2/3 axon	Thsd7a (5), Grik1 (5), Calb1 (5), Fstl4 (5), Gpr83 (5), Galntl6 (5), Ncam2 (5), Pcp4 (4), Cnr1 (2), Grm7 (1)
Pvalb	L4 axon	Parm1 (5), Lrrtm4 (5), Cntnap5c (4), Rab3b (3), Neto1 (3), Lin7a (3), Cdh9 (3), Gpr123 (3), Ddn (3), Cort (2)
Pvalb	L5 axon	Pcp4 (5), Grm7 (4), Ncam2 (4), Calb1 (3), Spint2 (3), Sphkap (3), Col14a1 (3), Cdh4 (2), Sgcz (2), Dgkb (2)
Pvalb	L6 axon	Sema3e (5), Chrm2 (5), Galntl6 (5), Kcnc2 (4), Rasgrf1 (4), Prdm8 (4), Thsd7a (3), Cnih3 (3), Lgals1 (3), Lypd6b (2)
Pvalb	L1 dendrite	Myh7 (5), Igf1 (4), Thsd7a (4), Rgs14 (4), Oprm1 (4), Sstr2 (3), Fam19a1 (3), Itpka (3), Kctd4 (2), Adcyap1 (2)
Pvalb	L2/3 dendrite	Thsd7a (5), Col25a1 (5), Calb1 (5), Ncam2 (4), Galntl6 (4), Cnr1 (4), Cdh13 (4), Pcp4 (3), Ntng1 (3), Npas3 (2)
Pvalb	L4 dendrite	Gpr123 (5), Rab3b (5), Parm1 (5), Cntnap5c (4), Cdh7 (3), Chrna7 (3), Ntrk3 (3), Neto1 (2), Cdh9 (2), Olfm3 (2)
Pvalb	L5 dendrite	Calb1 (5), Zbtb20 (4), Pcp4 (4), Dgkb (4), Tmem196 (4), Nell1 (4), Npas3 (4), 9630002D21Rik (3), Popdc3 (2), Kcnip2 (2)
Pvalb	L6 dendrite	Gpr83 (5), Chrm2 (5), Sema3e (5), Rbp4 (5), Fstl4 (4), Rasgrf1 (3), Lrp1b (3), Synpr (2), Ptprk (2), Fam19a5 (2)
Pvalb	soma depth	Thsd7a (5), Sema3e (5), Galntl6 (5), Fstl4 (5), Chrm2 (5), Gpr83 (4), Edil3 (4), Col25a1 (4), Calb1 (4), Lypd6b (2)
Pvalb	axon centroid	Fstl4 (5), Chrm2 (5), Sema3e (4), Col25a1 (4), Thsd7a (3), Galntl6 (3), Kcnc2 (3), Gpr83 (3), Edil3 (2), Lypd6b (2)
Pvalb	dendrite centroid	Thsd7a (5), Gpr83 (4), Fstl4 (4), Chrm2 (4), Sema3e (3), Galntl6 (3), Edil3 (3), Col25a1 (2), Calb1 (2), Pcp4 (2)
Lamp5	l1 axon	Opcml (5), Timp2 (5), Tmem132d (4), Zbtb20 (3), Slc30a3 (3), Dner (3), Flt3 (3), Fstl4 (2), Ndst4 (2), Oxtr (2)
Lamp5	soma depth	Oprm1 (5), Cecr6 (4), Rnf152 (4), Rgma (3), Rap1gap2 (3), Tac1 (2), Timp2 (2), Slc44a5 (2), Frmd6 (2), Glt8d2 (2)
Lamp5	axon centroid	Cecr6 (5), Rap1gap2 (4), Oprm1 (4), Slc44a5 (3), Rnf152 (3), Ntn5 (2), Timp2 (2), Slc32a1 (2), Glt8d2 (2), Rgma (2)
Lamp5	dendrite centroid	Cecr6 (4), Oprm1 (4), Rnf152 (3), Cplx3 (3), Glt8d2 (3), Tnnt1 (2), Cdca7 (2), Grm1 (2), Rap1gap2 (2), Nrgn (2)
Vip	L1 axon	Rbfox1 (5), Gulp1 (5), Yap1 (4), Pld5 (4), LOC105245190 (4), Csgalnact1 (3), Klk8 (2), Stard13 (2), Adarb2 (2), Anxa11 (2)
Vip	L2/3 axon	Kcnmb4 (5), Parm1 (5), Kirrel3 (5), Cdh13 (4), Isoc1 (4), Fndc5 (3), Kit (2), Ano3 (2), Ppapdc1a (2), Npy (2)
Vip	L4 axon	Prr16 (5), Kcnip4 (5), Elmo1 (4), Rin1 (3), Ptger3 (3), Timp2 (2), Fam19a2 (2), Arhgef28 (2), Hspb3 (2), Igsf11 (2)
Vip	L5 axon	Npy2r (5), Kcnmb4 (5), Parm1 (4), Ano3 (3), Col24a1 (2), Kirrel3 (2), Map3k5 (2), Mpped2 (2), Ccdc80 (2), Dner (1)
Vip	L2/3 dendrite	Bhlhe40 (5), Cort (5), Kirrel3 (5), Slc10a4 (4), Sfrp2 (4), Wnt7a (3), Gap43 (2), Sorcs2 (2), Kit (2), Synpr (2)
Vip	l4 dendrite	Kirrel3 (5), Bhlhe40 (5), Wnt2 (4), Lin7a (3), Nxph4 (3), Elmo1 (3), Myh14 (3), Cdh13 (2), Crhr1 (2), Grp (2)
Vip	l5 dendrite	Tmem132e (5), Sfrp2 (5), Kirrel3 (5), Kit (4), Lhx6 (3), Islr2 (3), LOC105244000 (2), Ccdc80 (2), Col24a1 (2), 6330403A02Rik (2)
Vip	soma depth	Kirrel3 (5), Rln1 (4), Anxa11 (4), Synpr (4), Megf10 (4), Chrm3 (2), Sfrp2 (2), Cntn5 (2), Eya4 (2), Fndc5 (1)
Vip	axon centroid	Kirrel3 (5), Rln1 (5), Ppapdc1a (4), Npy2r (4), Sfrp2 (3), Syt6 (3), Kit (2), Parm1 (2), Cort (2), Eya4 (2)
Vip	dendrite centroid	Kirrel3 (5), Sfrp2 (4), Rln1 (3), Ppapdc1a (3), Adra1b (3), Islr2 (3), Megf10 (2), Cdh13 (2), Chrm3 (1), Pbx3 (1)

Table S3: Gene sets selected via sparse linear regression for different cell types/subclasses and anatomical features. Only statistically significant sets are shown (See Table S1). Numbers in parentheses denote the number of times the preceding gene was selected out of 5 cross-validation runs.

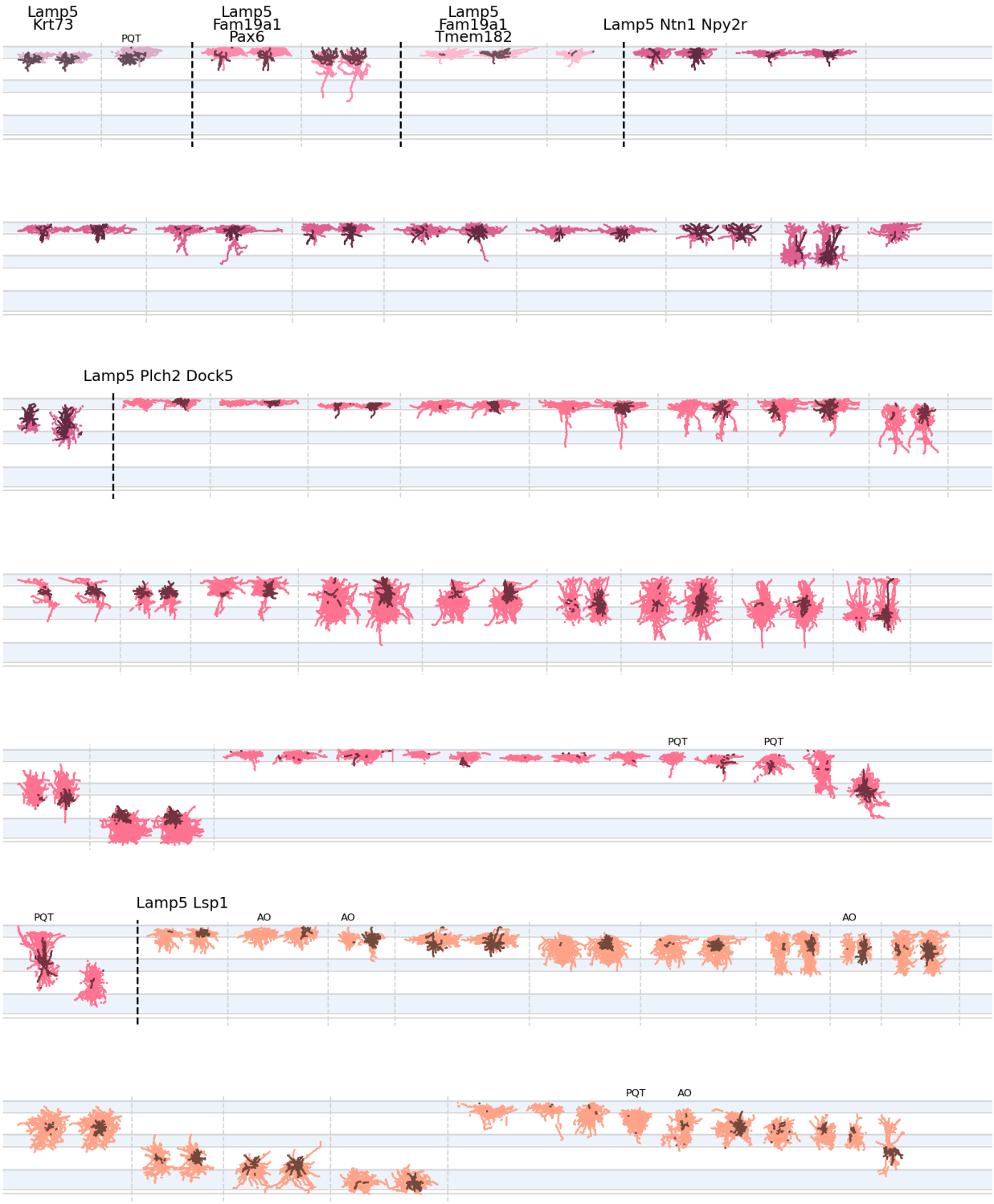

Figure S1: **Morphological reconstructions of inhibitory neurons ordered by t-type – 1 of 11.** 528 neurons have both automated and manual reconstructions, 274 - only automated ones. For each t-type, cells with both automated and manual reconstructions are shown first, separated by faint dashed lines, followed by cells that are reconstructed only automatically. Dendrites and axon are in darker and lighter colors, respectively. Best viewed digitally. AO: cell used for arbor density based analysis only, not for feature based analysis. PQT: poor quality transcriptomic characterization – not used for t-type related analyses. T: cells used in segmentation model training.

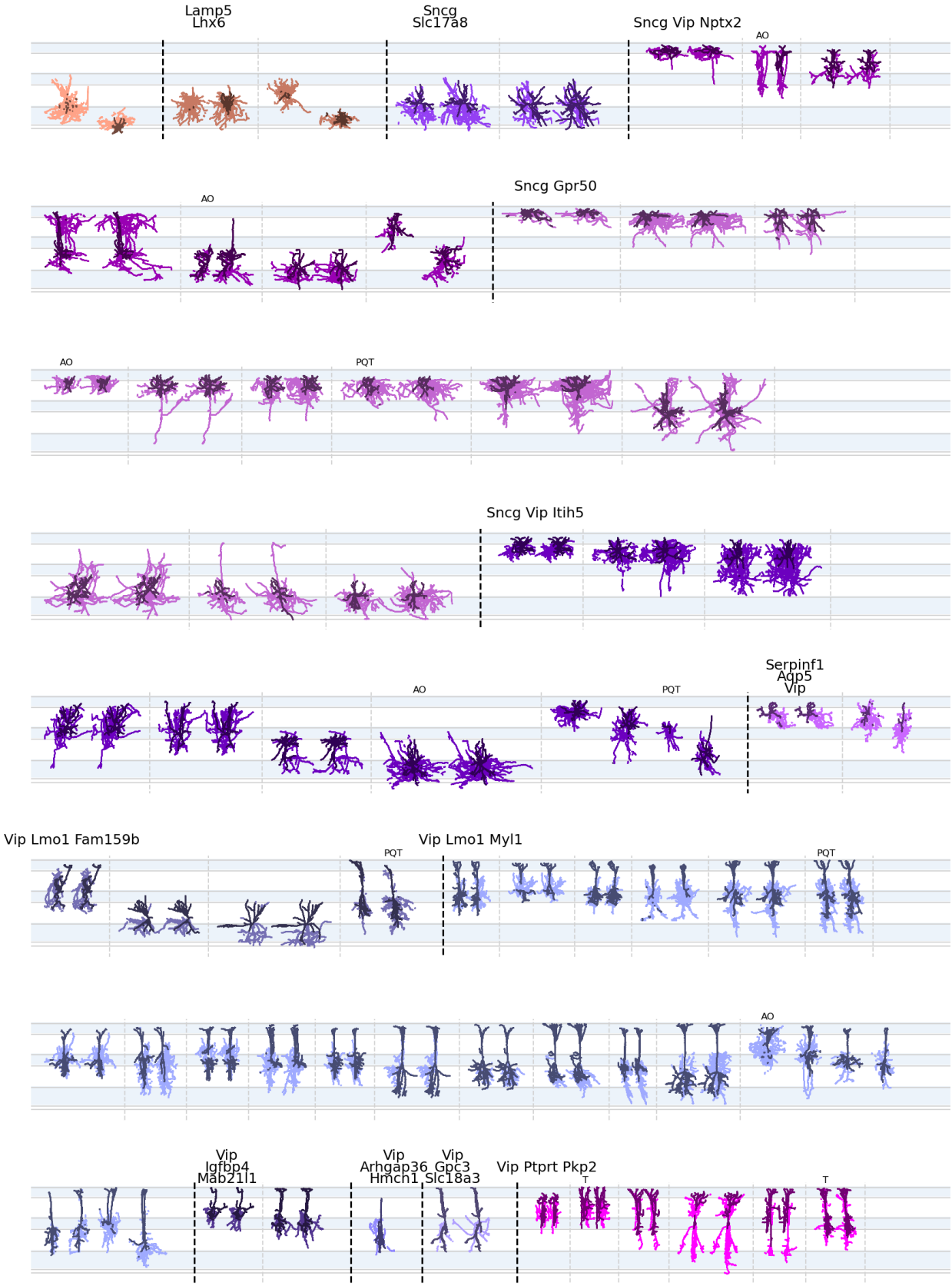

Figure S2: **Morphological reconstructions of inhibitory neurons ordered by t-type – 2 of 11.** Please refer to the caption of Figure S1.

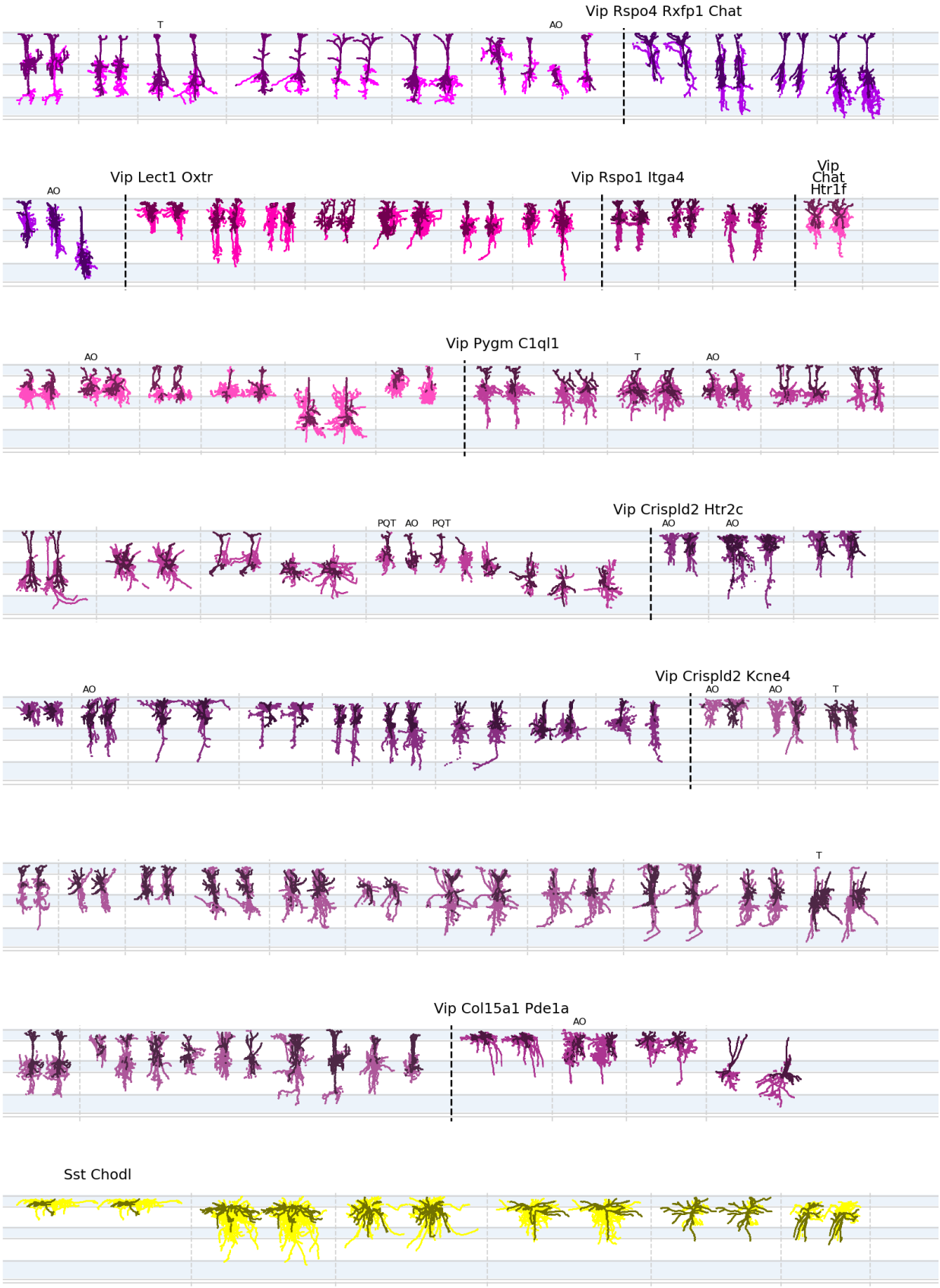

Figure S3: **Morphological reconstructions of inhibitory neurons ordered by t-type – 3 of 11.** Please refer to the caption of Figure S1

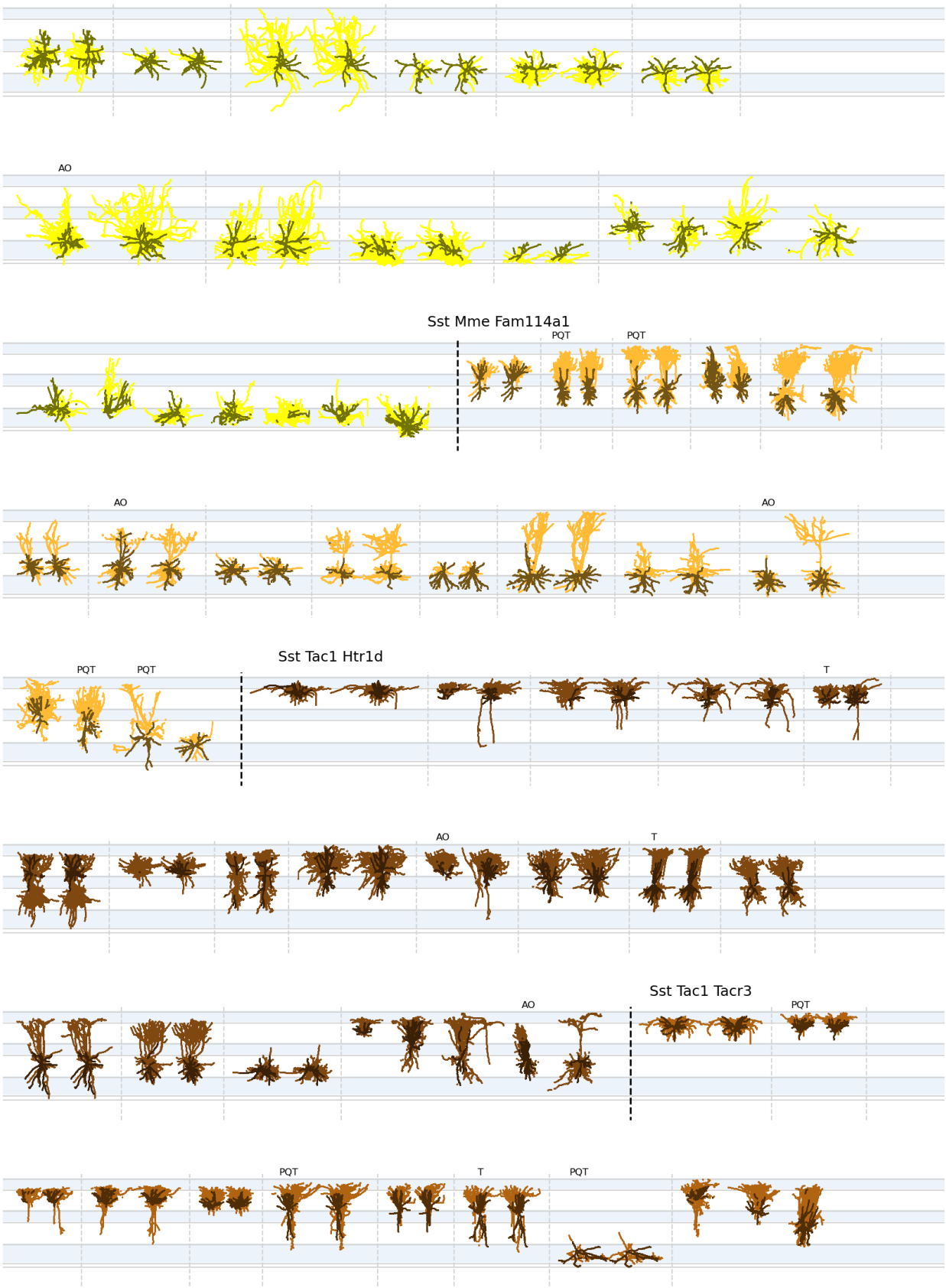

Figure S4: **Morphological reconstructions of inhibitory neurons ordered by t-type – 4 of 11.** Please refer to the caption of Figure S1

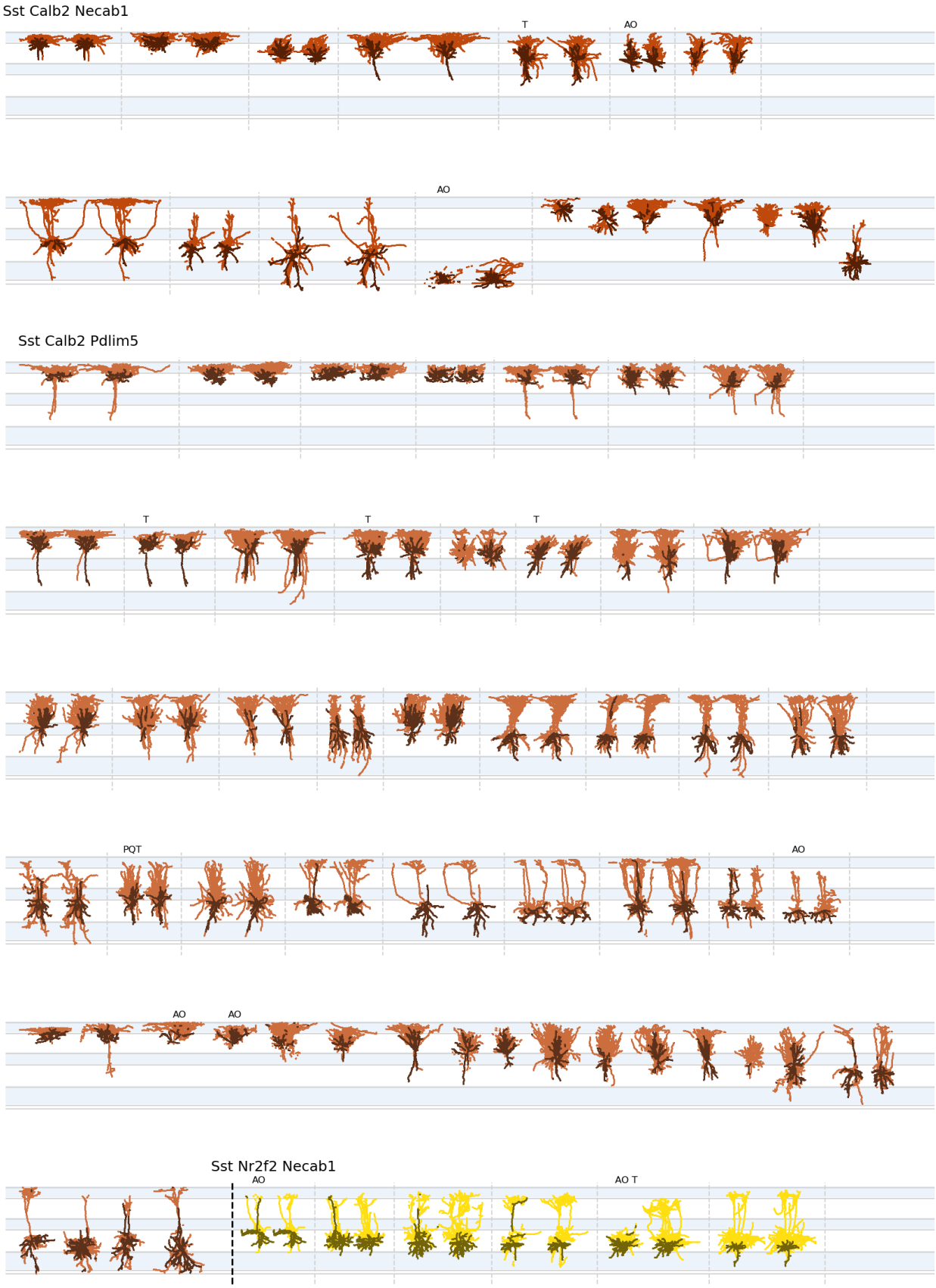

Figure S5: **Morphological reconstructions of inhibitory neurons ordered by t-type – 5 of 11.** Please refer to the caption of Figure S1

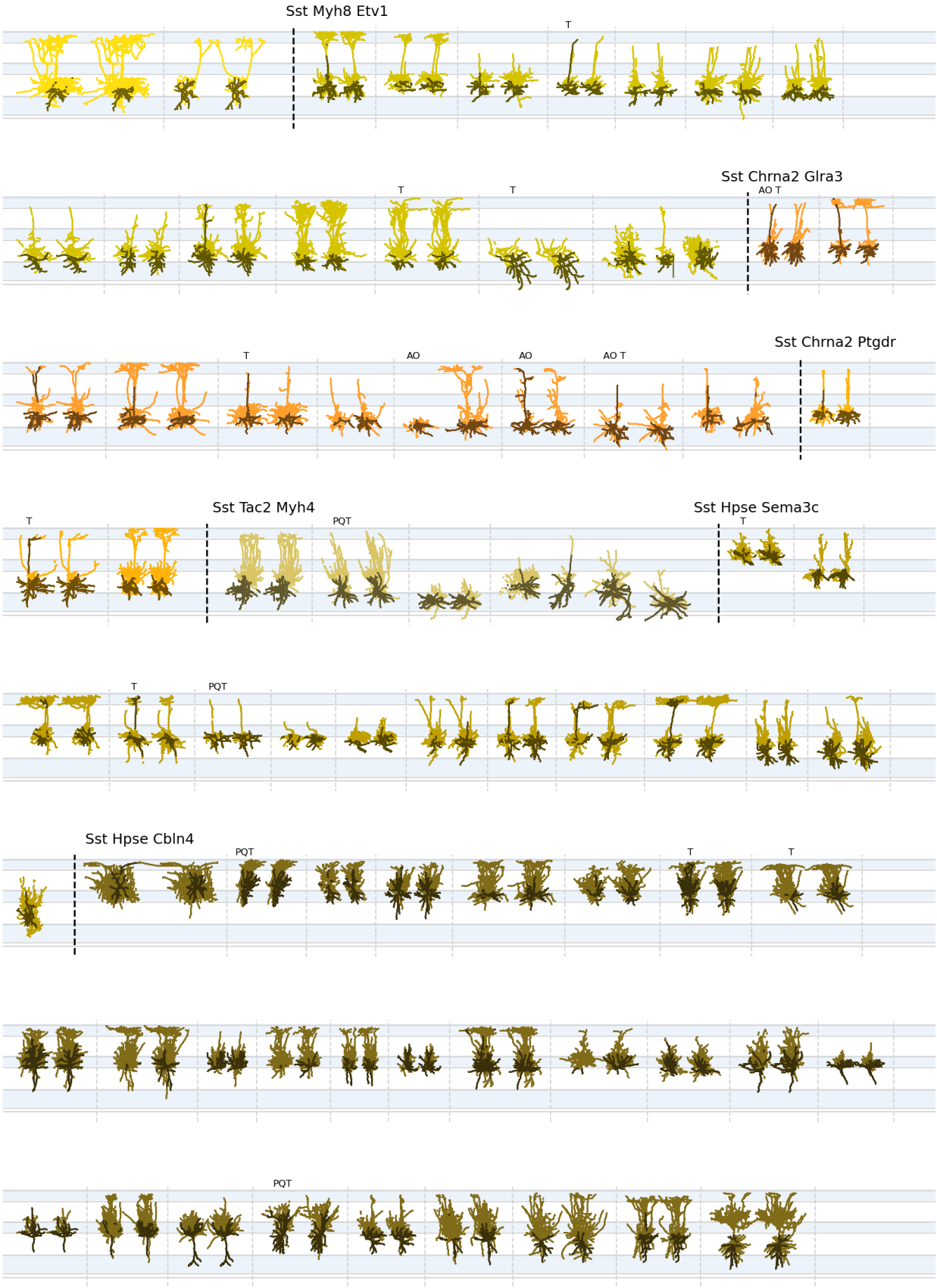

Figure S6: **Morphological reconstructions of inhibitory neurons ordered by t-type – 6 of 11.** Please refer to the caption of Figure S1

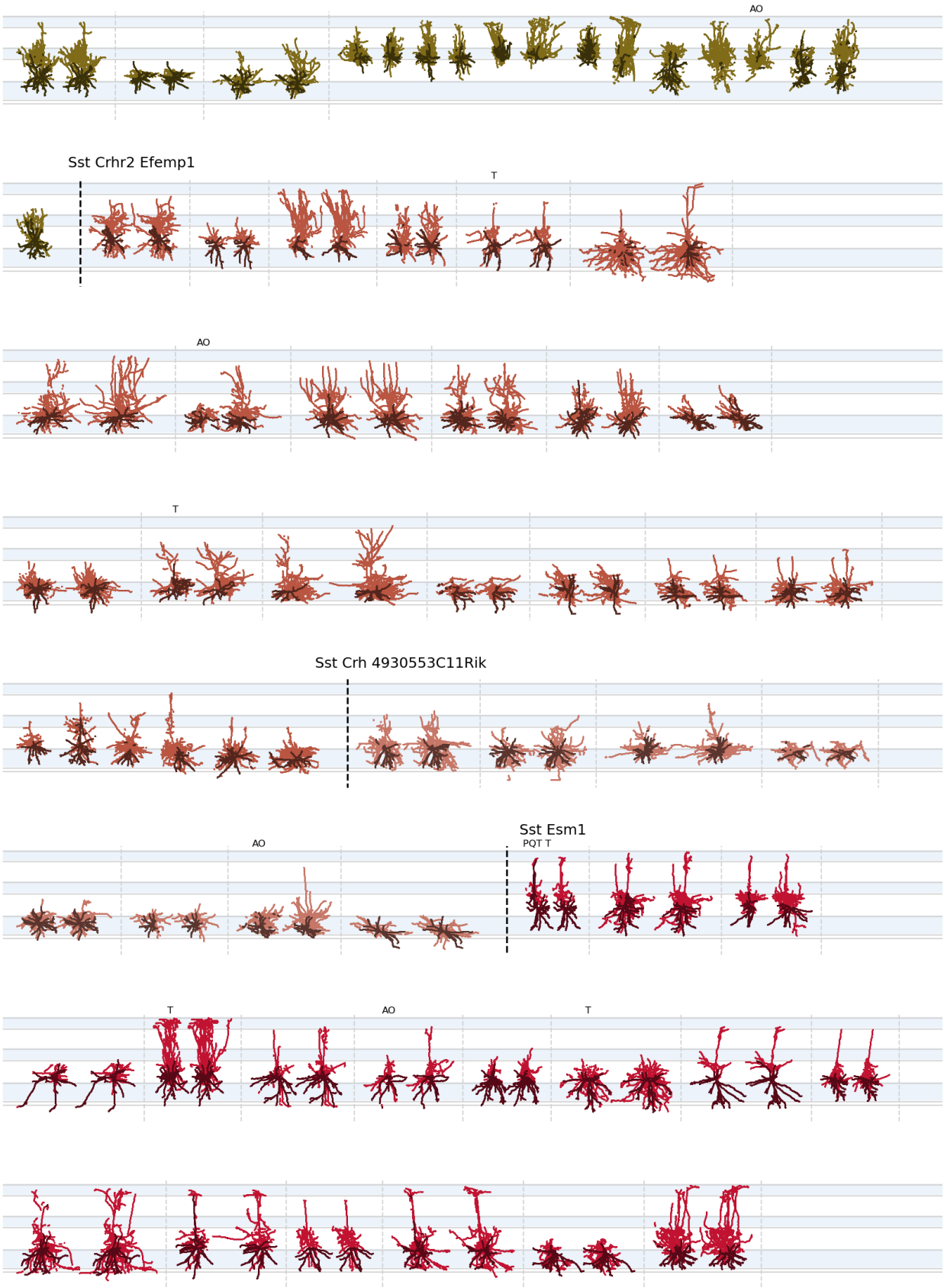

Figure S7: **Morphological reconstructions of inhibitory neurons ordered by t-type – 7 of 11.** Please refer to the caption of Figure S1

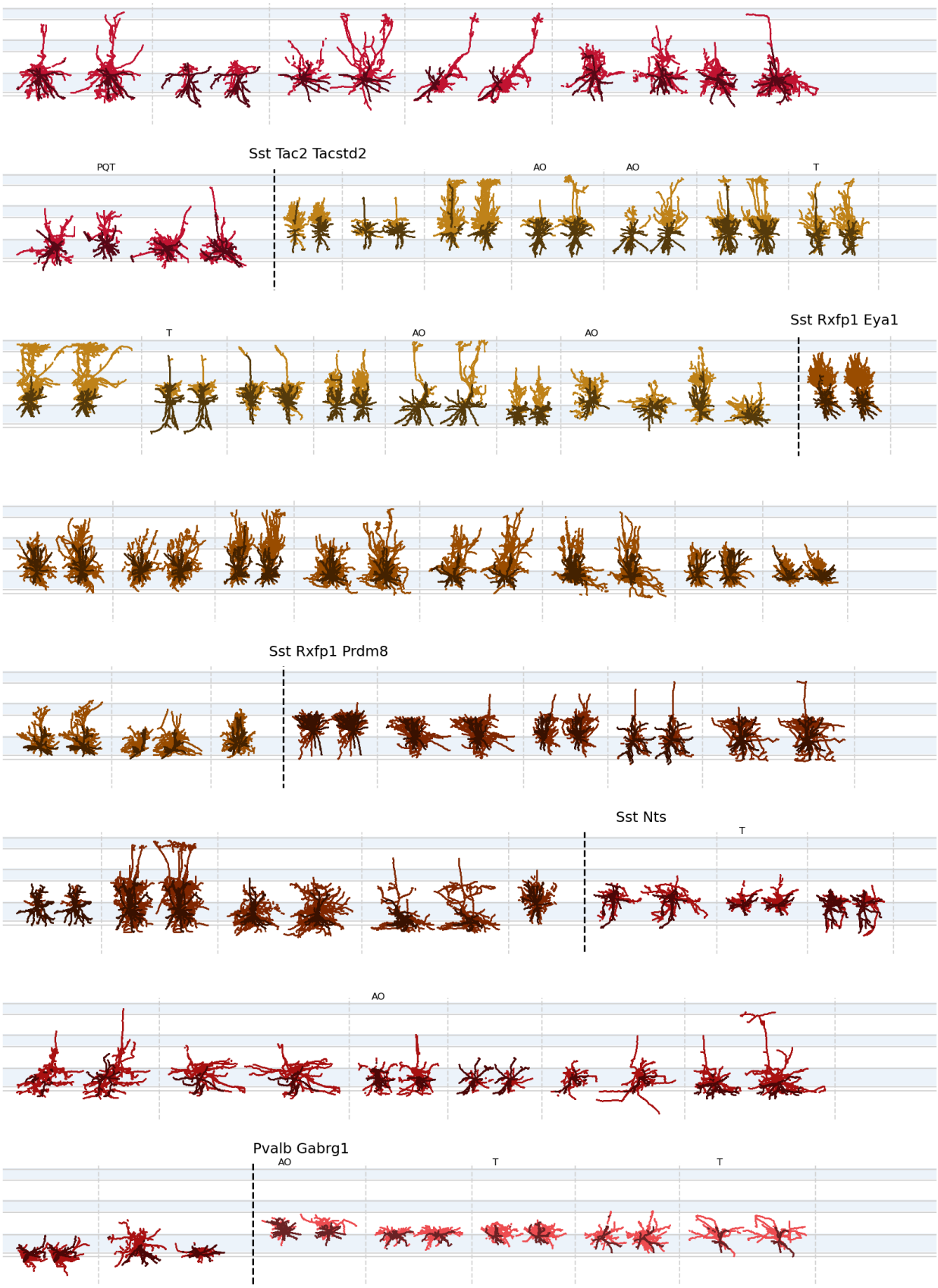

Figure S8: **Morphological reconstructions of inhibitory neurons ordered by t-type – 8 of 11.** Please refer to the caption of Figure S1

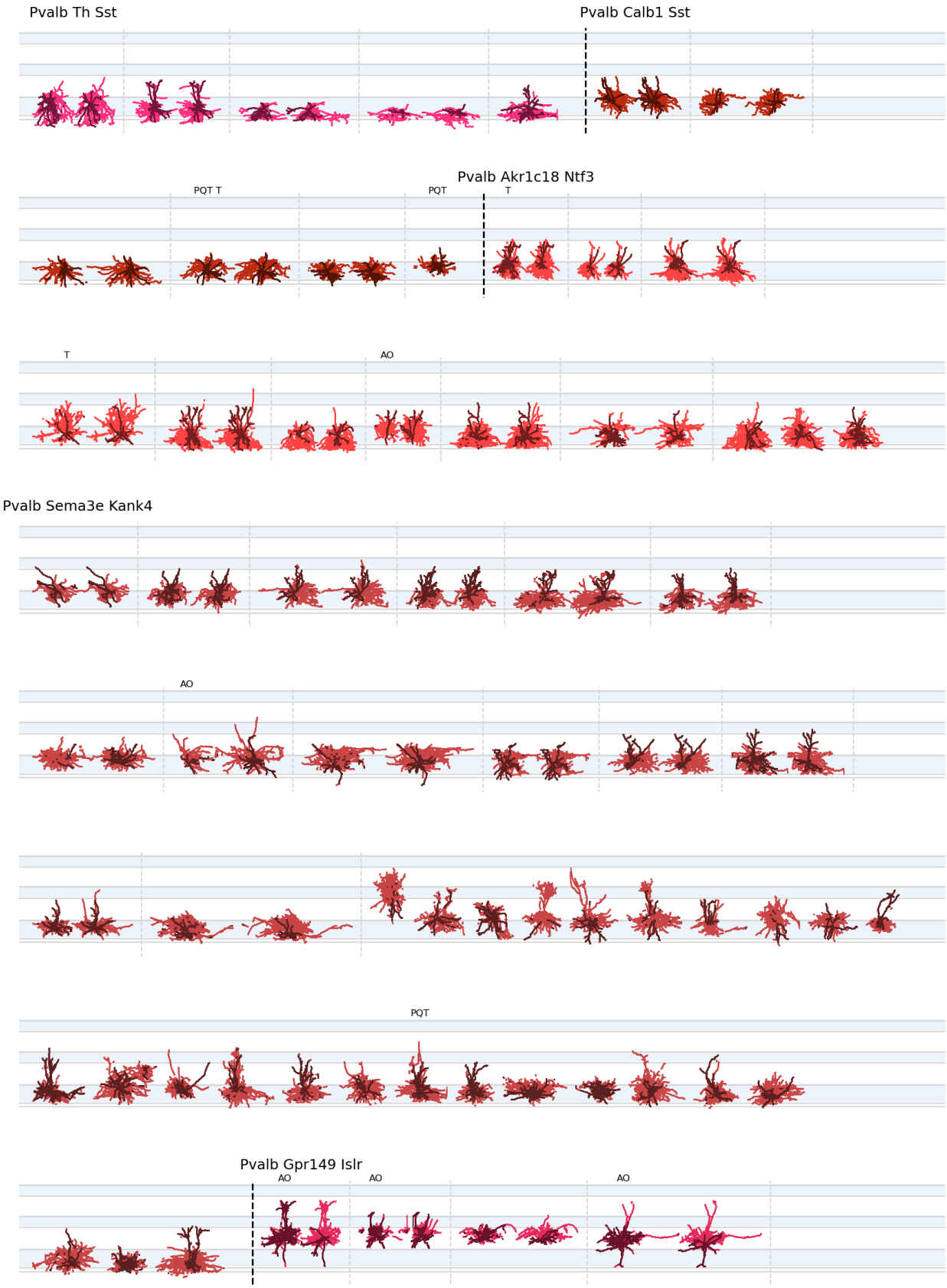

Figure S9: **Morphological reconstructions of inhibitory neurons ordered by t-type – 9 of 11.** Please refer to the caption of Figure S1

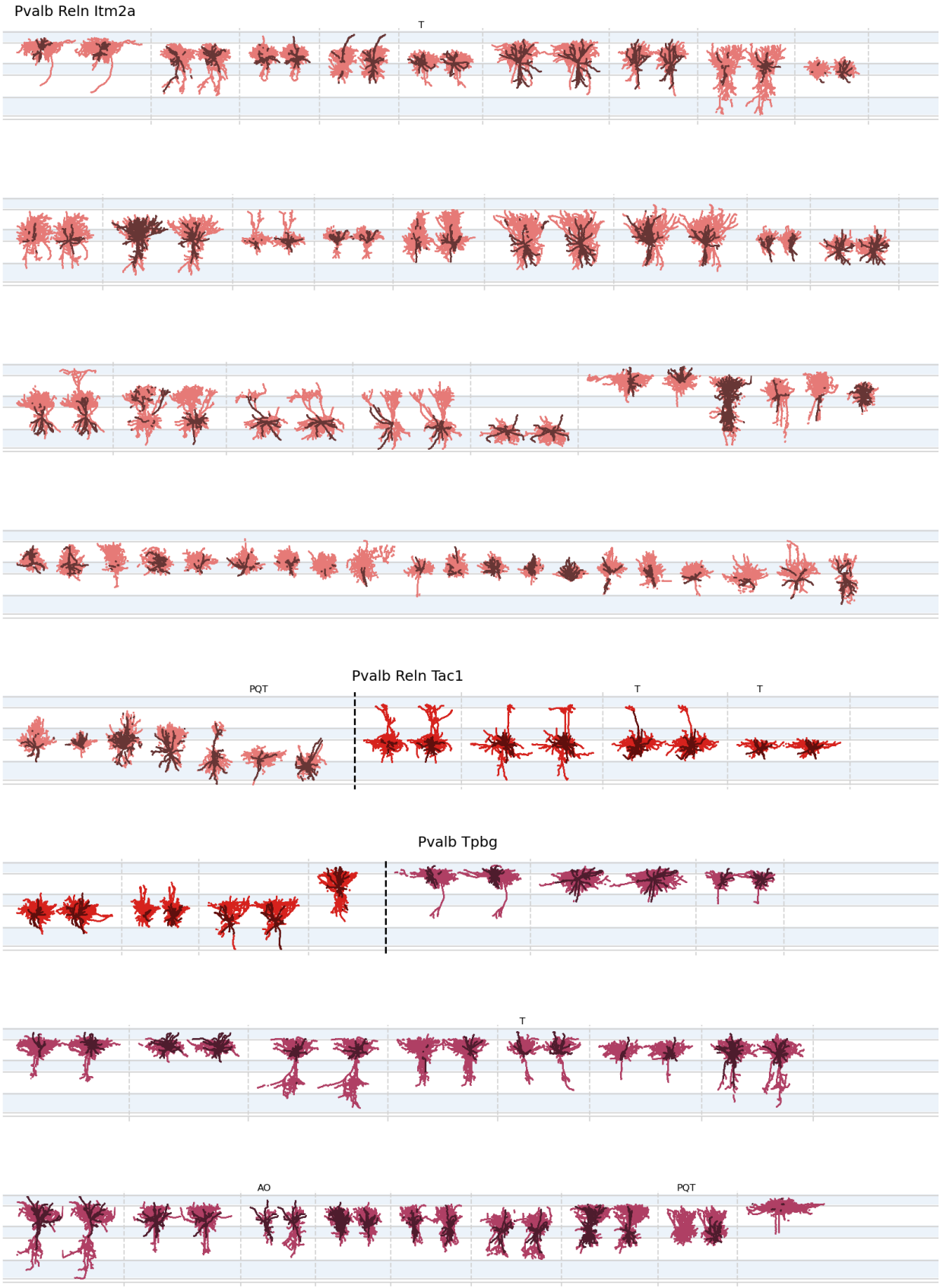

Figure S10: **Morphological reconstructions of inhibitory neurons ordered by t-type – 10 of 11.** Please refer to the caption of Figure S1

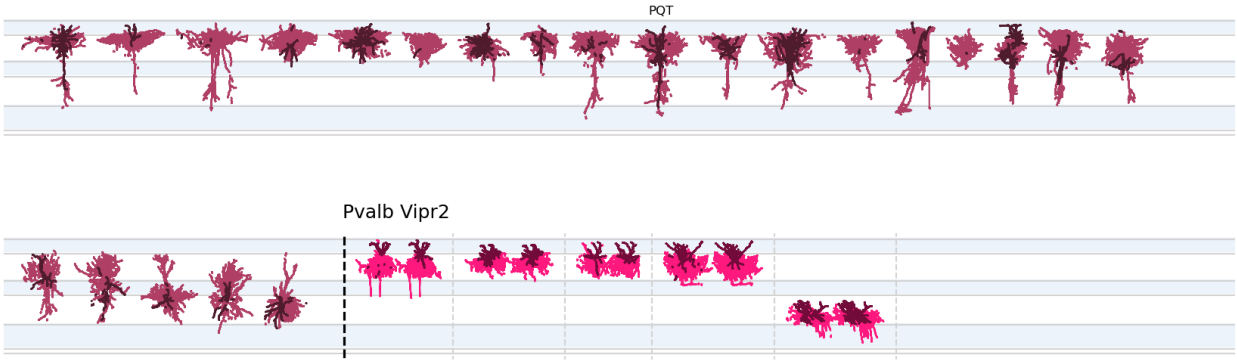

Figure S11: **Morphological reconstructions of inhibitory neurons ordered by t-type – 11 of 11.** Please refer to the caption of Figure S1

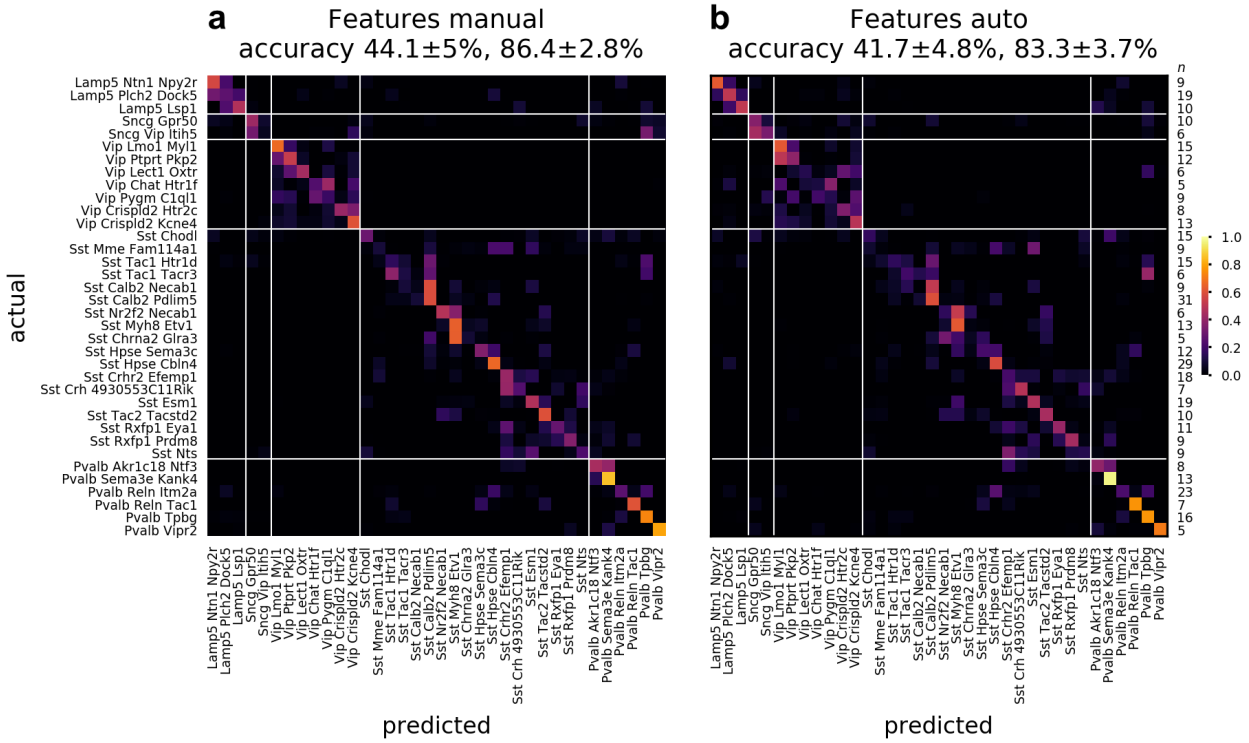

Figure S12: **Comparison of cell type classification accuracy based on a set of classical morphometric features using manually vs automatically reconstructed cells.** Confusion matrix for the classification of t-types based on features, using 427 manually (**a**) and automatically (**b**) reconstructed cells. Accuracy values reported in the headers refer to mean ± s.d. of the overall t-type and t-subclass classifiers, respectively, across cross-validation folds. Rightmost column lists the number of cells in each t-type (n).

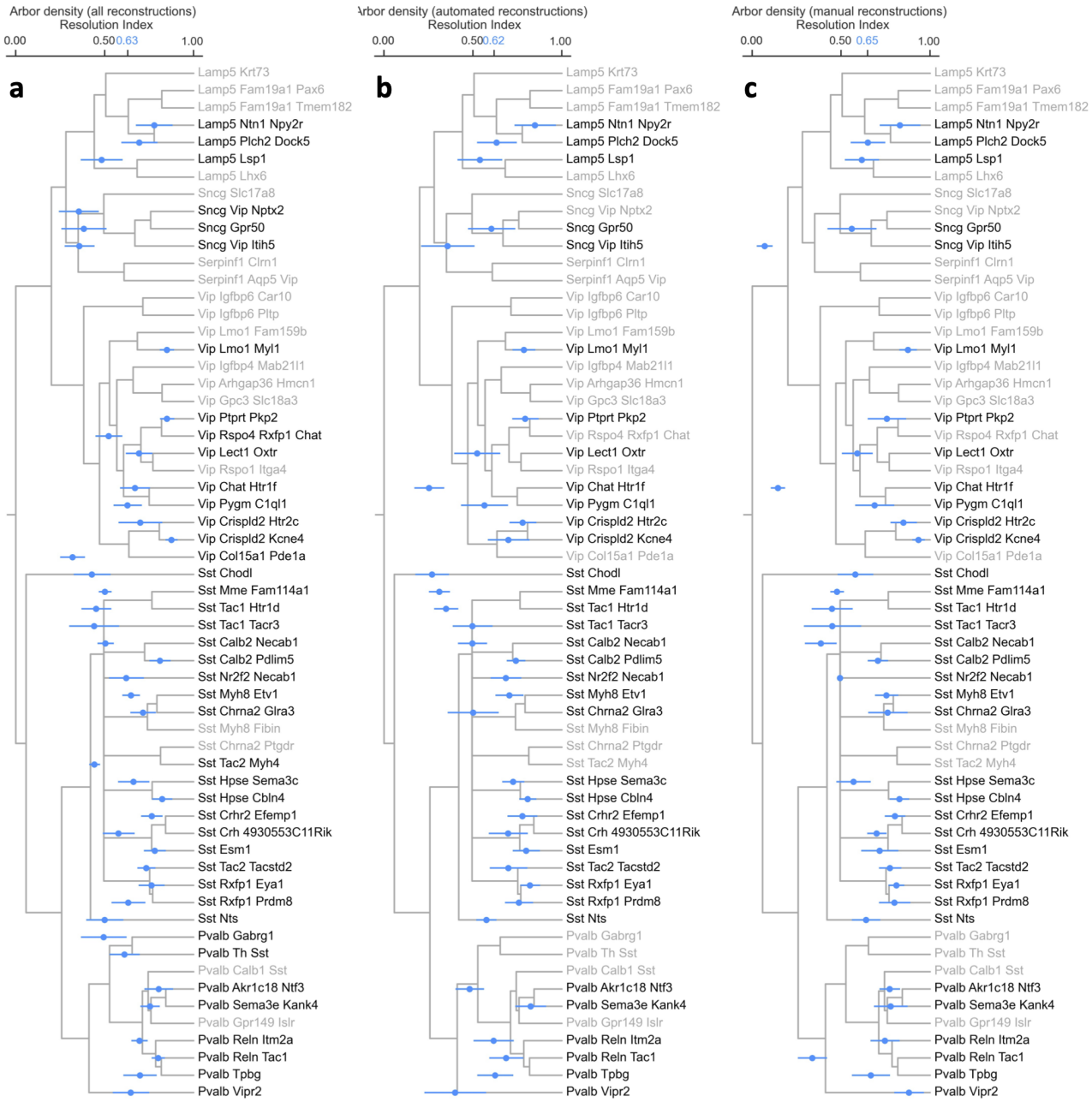

Figure S13: **Arbor density-based cell type classification performance using resolution index.** The depth of the Tasic et al. GABAergic neuron hierarchical tree is normalized to the 0-1 range, and resolution index for each cell is defined as the value of the closest common ancestor of the true and predicted leaf node labels. Perfect classification corresponds to resolution index of 1. Error bars indicate resolution index (mean ± SE over 10-fold stratified cross validation sets) for each cell type. The overall mean across cell types is indicated by blue on the y-axis. Cell types absent from the dataset are indicated by grayed out labels on the x-axis. Classification was performed with multi-layer perceptron classifiers using arbor density representation of all (**a**), automatically (**b**) and manually (**c**) reconstructed neurons as input. Resolution index values are not strictly comparable across panels because the numbers of cells and types are not identical. (See Figure 2.)

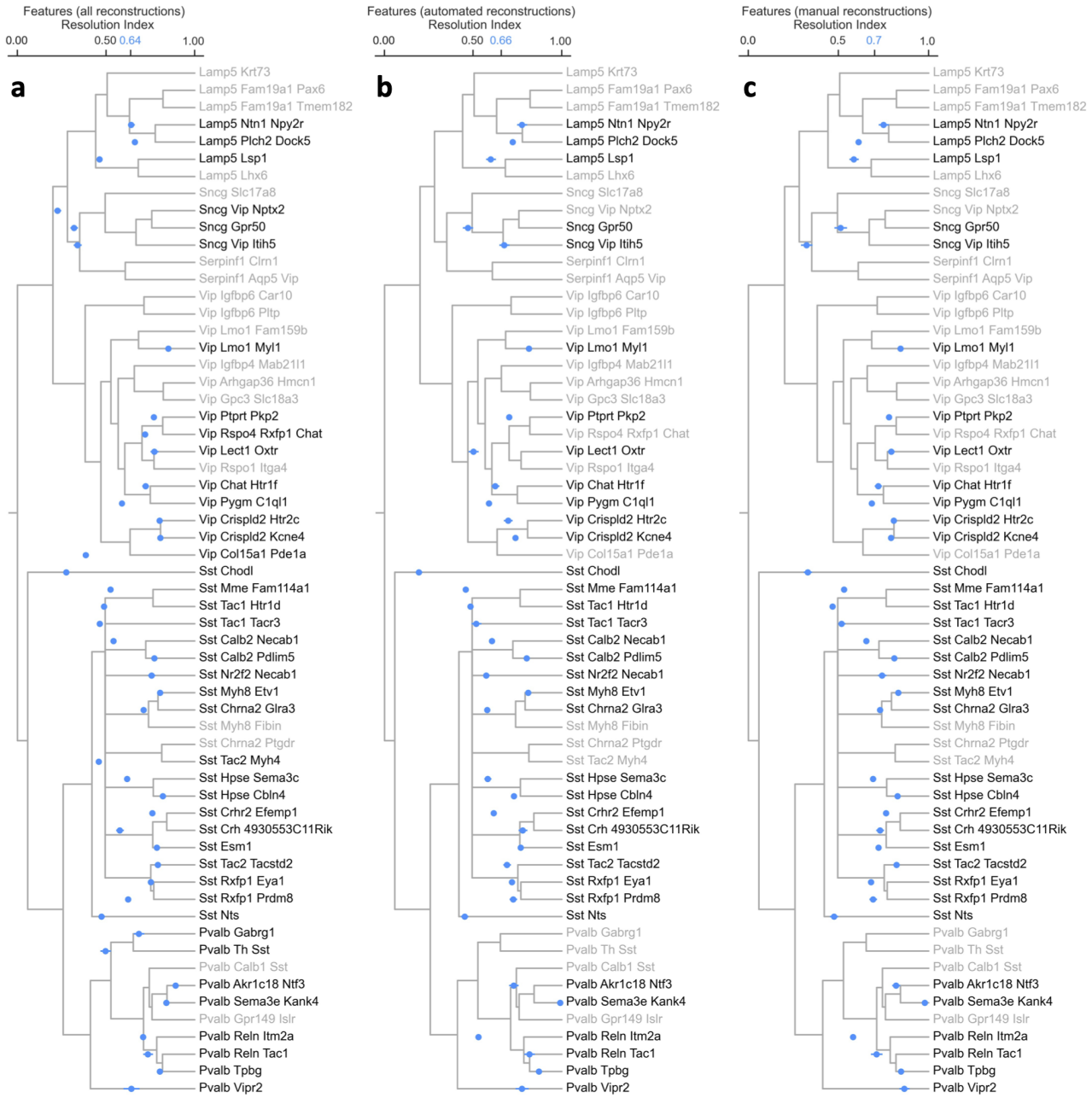

Figure S14: **Feature-based cell type classification performance using resolution index.** As before, error bars indicate resolution index (mean ± SE over 5-fold stratified cross validation sets repeated 20 times) for each cell type. The overall mean across cell types is indicated by blue on the y-axis. Cell types absent from the dataset are indicated by grayed out labels on the x-axis. Classification was performed with random forest classifiers using morphological features of all (**a**), automatically (**b**) and manually reconstructed cells (**c**) as input. Resolution index values are not strictly comparable across panels because the numbers of cells and types are not identical. (See Figure 2.)